

Equation of State and Progenitor Dependence of Stellar-Mass Black-Hole Formation

ANDRÉ DA SILVA SCHNEIDER,¹ EVAN O’CONNOR,¹ ELVIRA GRANQVIST,¹ AUREORE BETRANHANDY,¹ AND SEAN M. COUCH^{2,3,4,5}

¹*The Oskar Klein Centre, Department of Astronomy, Stockholm University, AlbaNova, SE-106 91 Stockholm, Sweden*

²*Department of Physics and Astronomy, Michigan State University, East Lansing, MI 48824, USA*

³*Department of Computational Mathematics, Science, and Engineering, Michigan State University, East Lansing, MI 48824, USA*

⁴*Joint Institute for Nuclear Astrophysics-Center for the Evolution of the Elements, Michigan State University, East Lansing, MI 48824, USA*

⁵*National Superconducting Cyclotron Laboratory, Michigan State University, East Lansing, MI 48824, USA*

(Dated: January 29, 2020)

ABSTRACT

The core collapse of a massive star results in the formation of a proto-neutron star (PNS). If enough material is accreted onto a PNS it will become gravitationally unstable and further collapse into a black-hole (BH). We perform a systematic study of failing core-collapse supernovae in spherical symmetry for a wide range of presupernova progenitor stars and equations of state (EOSs) of nuclear matter. We analyze how variations in progenitor structure and the EOS of dense matter above nuclear saturation density affect the PNS evolution and subsequent BH formation. Comparisons of core-collapse for a given progenitor star and different EOSs show that the path traced by the PNS in mass-entropy phase space $M_{\text{grav}}^{\text{PNS}} - \tilde{s}$ is well correlated with the progenitor compactness and almost EOS independent, apart from the final endpoint. Furthermore, BH formation occurs, to a very good approximation, soon after the PNS overcomes the maximum *gravitational* mass supported by a hot NS with constant entropy equal to \tilde{s} . These results show a path to constraining the temperature dependence of the EOS through the detection of neutrinos from a failed galactic supernova.

Keywords: black hole physics – equation of state – hydrodynamics – stars: evolution – stars: neutron – supernovae: general

1. INTRODUCTION

The existence of stellar mass black-holes (BHs) has long been inferred from observations of X-ray transients (Kubota et al. 1998; Esin et al. 1998; Belczynski et al. 2012; Wiktorowicz et al. 2013) and has recently been boosted by multiple gravitational wave (GW) detections of binary BH mergers (Abbott et al. 2019a). The most likely channels in which these BHs form involve the core collapse of massive stars with zero-age main sequence (ZAMS) masses in the range $10 M_{\odot} \lesssim M_{\text{ZAMS}} \lesssim 100 M_{\odot}$ (Burrows 1988; O’Connor & Ott 2011). These massive stars may form binary BH systems when found in dense stellar systems (Portegies Zwart & McMillan 2000; Rodriguez et al. 2015) or when they have low metallicities and share a common envelope evolution (Belczynski et al. 2016; Mandel & de Mink 2016; Stevenson et al. 2017; Vitale et al. 2017).

The overall picture of how these stellar mass BHs come to be is well understood, even if some of the details are still not. At the end of their nuclear fusion cycle, the electron-

degenerate iron core of massive stars grows in mass from the ash of the silicon shell burning happening just outside the core. When it surpasses the effective Chandrasekhar mass, which not only depends on the electron fraction of the core but also its thermal structure (Woosley et al. 2002), the gravitational force becomes too strong to resist and the core collapses. During collapse, stellar core density increases by several orders of magnitude until nuclear densities are reached. At this stage, the equation of state (EOS) stiffens, core collapse momentarily halts forming a proto-neutron star (PNS) and sending a shock wave through the still infalling outer core. As the shock propagates it loses momentum and stalls due to photodissociation of heavy nuclei and neutrino losses (Colgate & White 1966; Bethe & Wilson 1985; Bethe 1990). Neutrino heating and other processes may revive the shock and unbind the stellar mantle resulting in a core-collapse supernova (CCSN) (Janka 2001, 2012; Ott et al. 2018). If the shock is not revived, or even if it is but not enough material is unbound, fallback accretion onto the PNS occurs until the repulsive nuclear forces cannot prevent another gravitational instability and the PNS collapses into a stellar-mass BH (Burrows 1986, 1988; O’Connor & Ott 2011).

The mechanisms by which CCSNe occur, their explosion energy and ejected mass, if any, all depends on yet poorly

constrained details of the equation of state (EOS) of dense matter (Lattimer 1981; Swesty et al. 1994; Lattimer & Prakash 2000; Hempel et al. 2012). For a given progenitor even small changes in the EOS (Schneider et al. 2019a) or neutrino transport (Melson et al. 2015; Burrows et al. 2018) may dictate whether a successful or failed supernova occurs. Thus, accurate predictions of the outcome of CCSNe can be quite difficult. Multidimensional simulations predict a variety of CCSN outcomes that include successful and failed explosions which, in the former, can lead to the formation of a NS or a BH (Janka 2012; Burrows et al. 2018; Ott et al. 2018; O’Connor et al. 2018; Pan et al. 2018; Obergaulinger & Aloy 2019; Burrows et al. 2020). However, because successful explosions depend on multidimensional physics, explosions in spherically symmetric simulations only occur for the lightest core-collapse progenitors, $M \lesssim 10 M_\odot$ (Kitaura et al. 2006; Fischer et al. 2010); or by artificially enhancing neutrino cross reaction rates (Fischer et al. 2010, 2012; Martínez-Pinedo et al. 2012), artificially driving PNS contraction (Ugliano et al. 2012; Ertl et al. 2016), or including approximate schemes to emulate multi-dimensional effects (Couch et al. 2019). Because our main interest is on PNS collapse into a BH, we limit our simulations to spherical symmetry without facilitating explosions.

In the current study we build upon the work of O’Connor & Ott (2011), which studied EOS effects in the failed collapse of 106 pre-SNe progenitor stars and 4 different EOSs. Here, we perform simulations of failed CCSNe using 49 EOSs from Schneider et al. (2019a) and 51 supernova progenitors selected from the works of Woosley et al. (2002), Woosley & Heger (2007), and Sukhbold et al. (2018). By performing a systematic study of failed CCSNe we are able to significantly improve upon our understanding of how different features of the EOS affect PNS evolution until the moment of BH formation. Works by Hempel et al. (2012); Yasin et al. (2018); Schneider et al. (2019a) hint that the temperature dependence of the EOS may be the main source of uncertainty in the outcome of CCSNe. Particularly, Hempel et al. (2012); Steiner et al. (2013) found, studying the collapse of a single pre-SN progenitor and 7 different EOSs, that the time for BH formation during a failed core-collapse and its initial gravitational mass is proportional to the maximum gravitational mass supported by a NS with constant entropy $s = 4 k_B \text{ baryon}^{-1}$. From our set of simulations we are able to explain the results seen in many previous works of the relations between the EOS of dense matter and progenitor structure and BH formation, including Sumiyoshi et al. (2009); O’Connor & Ott (2011); Nakazato et al. (2012); Hempel et al. (2012); Steiner et al. (2013); Char et al. (2015); Pan et al. (2018). Furthermore, we show that some characteristics of failed core-collapse are mostly progenitor dependent, *i.e.*, almost EOS independent, while others depend as much on the zero-temperature EOS as on its finite-temperature components.

This work is structured as follows. In Sec. 2 we discuss the pre-supernova progenitor stars, the EOSs, and the setup of our simulations. We perform the bulk of our simulations

using a general relativistic effective potential (GREP). Thus, to test the accuracy of this approach we compare BH formation scenarios using a GREP to full general relativistic calculations in Sec. 3. Results of our simulations and insight gained from them are discussed in Sec. 4. We conclude in Sec. 5.

2. MODEL

2.1. Progenitors

In our study, we perform core collapse simulations for 51 different progenitor stars and analyze PNS evolution up to the point of BH formation. For our main results, we analyze six progenitor stars compiled from Woosley et al. (2002) and Woosley & Heger (2007) and listed in Table 1. These progenitors cover a wide range of compactnesses $0.2 \lesssim \xi_{2.5} \lesssim 0.9$ as defined by O’Connor & Ott (2011),

$$\xi_M = \frac{M/M_\odot}{R(M_{\text{baryon}} = M)/1000 \text{ km}} \Big|_{t=t_0}. \quad (1)$$

The compactness ξ_M of a pre-SN progenitor star is, to first order, connected to the time it takes for the coordinate mass M to be accreted by a newly formed PNS (O’Connor & Ott 2011). Thus, ξ_M is also a good indicator of the time for the PNS to collapse into a BH provided we set $M \simeq M_{\text{max}}^{\text{PNS}}$, where $M_{\text{max}}^{\text{PNS}}$ is the maximum mass that can be supported by the PNS. Following O’Connor & Ott (2011), we take $M = 2.5M_\odot$. The compactness, $\xi_{2.5}$, may be computed at different times during the stellar evolution. While we use the values from pre-SN progenitors at the start of collapse, $t_0 = 0$, so that the values are independent of the EOS used to simulate the core collapse, O’Connor & Ott (2011) compute $\xi_{2.5}$ at the moment of core bounce, $t = t_{\text{bounce}}$ and, thus, their values are sensitive to the EOS. Therefore, the values quoted here for $\xi_{2.5}$ may differ from the ones of O’Connor & Ott (2011) for the same progenitor. These differences become larger the more compact the progenitor is.

We simulate the collapse of the six progenitor stars of Woosley et al. (2002) and Woosley & Heger (2007) using 49 unique EOSs of Schneider et al. (2019a), discussed below. Furthermore, we add to our analysis data from the core-collapse of 45 progenitors from Sukhbold et al. (2018) that were produced with a reduced (to 1/10 of the default value) mass loss rate and ZAMS masses in the range of $16 M_\odot \leq M \leq 60 M_\odot$ in increments of $1 M_\odot$. These pre-SN progenitors cover compactness in the range $0.15 \lesssim \xi_{2.5} \lesssim 0.65$. For the simulations performed with these 45 progenitors we use a single EOS. These simulations are run to test the insights gained from the simulations using the six progenitors in Table 1 with many different EOSs and to test the impact of the effective gravitational potential on BH formation properties. The density profiles of the pre-SN progenitor stars are shown in Figure 1.

We focus on PNS evolution as a function of compactness due to our main interest lying in failed CCSNe and BH formation. Ertl et al. (2016); Ebinger et al. (2018) have shown that one characteristic parameter of the pre-SN progeni-

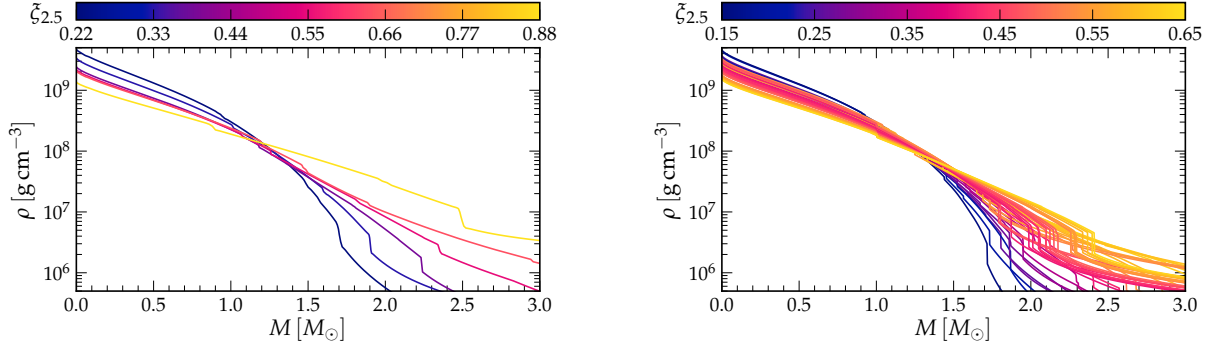


Figure 1. Density as a function of baryonic mass coordinate and compactness $\xi_{2.5}$, Equation (1). Plots are for six models from Woosley et al. (2002) and Woosley & Heger (2007) (left, see also Table 1) and 45 models of Sukhbold et al. (2018) with masses between $16-M_{\odot}$ and $60-M_{\odot}$ (right).

Table 1. Pre-SN progenitor name, zero age main sequence mass (M_{ZAMS}), total pre-supernova mass (M_{pre-SN}), iron core mass (M_{Fe}), and compactness parameters $\xi_{2.5}$ (O’Connor & Ott 2011). Models that start with the letter s have solar metallicity, u have 10^{-4} solar metallicity and z have zero metallicity. Models with WH07 and WHW02 in their name are from Woosley & Heger (2007) and Woosley et al. (2002), respectively. Compactness, $\xi_{2.5}$, values are for pre-SN progenitors at the start of collapse and, thus, differ from the ones of O’Connor & Ott (2011), which were computed for a single EOS at the moment of core bounce.

Name	M_{ZAMS} [M_{\odot}]	M_{pre-SN} [M_{\odot}]	M_{Fe} [M_{\odot}]	$\xi_{2.5}$
s50WH07	50	9.76	1.50	0.221
s25WH07	25	15.8	1.60	0.330
z25WHW02	25	25.0	1.81	0.389
s40WH07	40	15.3	1.83	0.544
u40WHW02	40	40.0	1.90	0.638
u75WHW02	75	74.1	2.03	0.879

tor star, such as the compactness, is not enough to address which progenitors lead to successful or failed CCSNe explosions. In fact, as we show in Section 4.3, stars with very similar compactnesses may have quite different accretion histories and, thus, particular likelihoods of leading to a successful explosion that depend on their structures.

2.2. Equations of State

For each of the progenitors from Woosley et al. (2002) and Woosley & Heger (2007) we run simulations using 49 unique EOSs from Schneider et al. (2019a) computed using the open-source code SROEOS of Schneider et al. (2017). These EOSs consider only nucleons (protons and neutrons) in the nuclear sector. Nuclear matter is assumed to be in thermal equilibrium with a background gas of photons, electrons, and positrons, and to be locally charge neutral. Starting from a baseline Skyrme-type EOS which agrees with current nuclear physics constraints (Margueron et al. 2018; Danielewicz 2002), see Table 2, Schneider et al. (2019a) con-

structed four sets of EOSs that vary in at most two experimentally accessible physical parameters: (1) set s_M varied the effective mass of nucleons; (2) set s_S varied the symmetry energy of nuclear matter and its slope; (3) set s_K varied the incompressibility of symmetric nuclear matter (SNM) and pure neutron matter (PNM); and (4) set s_P varied the pressure of SNM and PNM according to constraints of Danielewicz (2002).

In this work we focus on two EOS sets, s_M and s_P . Set s_M allows variations in the effective masses of SNM at nuclear saturation density, $m^* = m_n^*(n = n_{sat}, y = 1/2) \simeq m_p^*(n_{sat}, 1/2)$, and the effective-mass splitting for PNM, $\Delta m^* = m_n^*(n_{sat}, 0) - m_p^*(n_{sat}, 0)$. Here n is the baryon density, $n_{sat} = 0.155 \text{ fm}^{-3}$ the saturation density, and y the proton fraction, *i.e.*, the ratio of protons to nucleons. In Skyrme-type models, the effective mass is computed from

$$\frac{\hbar^2}{2m_t^*} = \frac{\hbar^2}{2m_t} + \alpha_1 n_t + \alpha_2 n_{-t}, \quad (2)$$

where α_i are parameters of the model, m_t and n_t are, respectively, the vacuum mass and the number density of nucleon of type t . If $t = n$ then $-t = p$ and vice versa. These EOSs were constructed such that all EOSs in set s_M have very similar zero-temperature components regardless of choice for m^* and Δm^* . The finite-temperature component of the EOS, on the other hand, is sensitive to the effective masses of nucleons (Prakash et al. 1997; Steiner et al. 2013; Constantinou et al. 2014) and, thus, differs amongst EOSs in set s_M .

The second set analyzed, s_P , allows variations in the pressure of zero-temperature SNM and PNM at $4n_{sat}$ based on constraints by Danielewicz (2002). The range of pressures allowed at $n = 4n_{sat}$ is such that all EOSs can produce cold non-rotating beta-equilibrated neutron stars (NSs) with gravitational mass $M_{grav} \geq 2 M_{\odot}$. We stress that all EOSs in set s_P have the same effective masses and, therefore, have the same contributions from the thermal component of the EOS. In sets s_M and s_P the effective masses and pressures at $n = 4n_{sat}$ can, respectively, vary from the baseline EOS values by $0, \pm 1$ and $\pm 2\sigma$ from their average values, see Table 2. Thus, each set contains 25 EOSs with the baseline EOS being present in both sets.

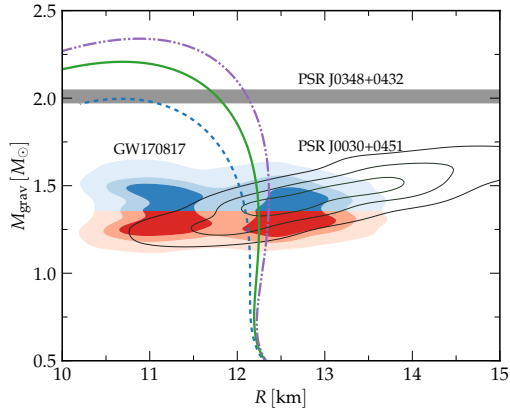


Figure 2. Mass-radius relationship for our baseline EOS and the softest and stiffest EOSs in set s_P . Also plotted are observational constraints from the LIGO-Virgo detection of GW170817 (Abbott et al. 2019b), the $2.01 \pm 0.04 M_\odot$ mass of PSR J0348+0432 as measured by Antoniadis et al. (2013), and the mass-radius of PSR J0030+0451 from the NICER collaboration (Miller et al. 2019). Different shades in the GW170817 data and the contour lines of the PSR J0030+0451 data denote the 50%, 68%, and 95% confidence intervals of the observations.

We focused on these two sets as variations in the effective mass (pressure) keeping pressure (effective mass) constant probe how core collapse and BH formation are affected by thermal (non-thermal) components of the EOS (Yasin et al. 2018; Schneider et al. 2019a,b). Often, EOSs are discussed in terms of their softness/stiffness. Here we make a distinction between what it means for an EOS to be soft or stiff depending on the set we are referring to. Since for set s_M the zero temperature component of the EOS is very similar for all EOSs in the set, we refer to the stiffest EOS to be the one where the pressure rises the fastest with increasing temperature. Meanwhile, for set s_P the temperature component of all EOSs is the same and, therefore, we refer to the stiffest EOS to be the one where the pressure rises the fastest with increasing density. The NS mass-radius relationship for our baseline EOS as well as the softest and the stiffest zero-temperature EOSs in set s_P are shown in Figure 2. By construction all EOSs in set s_M show very similar mass-radius curves (Schneider et al. 2019a). Finally, in order for all EOSs to have the same low density behavior, they are joined to an EOS of 3 335 nuclei in nuclear statistical equilibrium (NSE) at a transition density of $n_{\text{tr}} = 10^{-3} \text{ fm}^{-3}$ with width $n_\delta = 0.33$ (Schneider et al. 2017).

2.3. FLASH Simulation Setup

For our set of progenitors and EOSs we perform spherically symmetric core-collapse simulations using the FLASH simulation framework (Fryxell et al. 2000; Dubey et al. 2009). We use a similar FLASH setup to that of O’Connor et al. (2018) and Couch et al. (2019). We review some general features of FLASH here and point to references that contain further details about the code and systems of equations solved. In the

Table 2. Nuclear matter properties of our baseline EOS from constraints of Margueron et al. (2018), Nättilä et al. (2016), and Danielewicz (2002) and references therein, see Schneider et al. (2019a) for details. $1-\sigma$ variations used to compute EOS sets s_M and s_P are also shown.

Set	Quantity	Baseline	Variation σ	Unit
—	n_{sat}	0.155		fm^{-3}
—	ϵ_{sat}	−15.8		MeV baryon^{-1}
—	L_{sym}	32		MeV baryon^{-1}
—	K_{sat}	230		MeV baryon^{-1}
—	K_{sym}	−100		MeV baryon^{-1}
s_M	m^*	0.75	0.10	m_n
	Δm^*	0.10	0.10	m_n
s_P	$P_{\text{SNM}}^{(4)}$	125	12.5	MeV fm^{-3}
	$P_{\text{PNM}}^{(4)}$	200	20.0	MeV fm^{-3}

simulations, gravity is treated using an approximate general relativistic effective potential (Marek et al. 2006; O’Connor & Couch 2018a,b). The equations of motion of the system are solved using a newly-implemented hydrodynamics solver (Couch et al. 2019; Couch 2019) while neutrino transport is computed using the so-called “M1” transport (Shibata et al. 2011; Cardall et al. 2013; O’Connor 2015; O’Connor & Couch 2018a,b). Both the hydrodynamics and the radiation transport share a common time step that is set by the light-crossing time of the smallest grid zone and a Courant factor. We use a spherical grid with adaptive mesh refinement (AMR) for our simulations that extends out to $2 \times 10^9 \text{ cm}$. On the coarsest level there are 320 grid zones with a length of 62.5 km. We allow up to 10 total levels of refinement resulting in a smallest grid zone with a length of $\simeq 122 \text{ m}$. This small grid zone length improves modeling of the high density region near BH formation time. We use a Courant factor of 0.8 that results in a hydrodynamic time step of $\simeq 0.3 \times 10^{-6} \text{ s}$. We do two radiation substeps per hydrodynamic step and, therefore, the effective CFL factor for the radiation substeps is 0.4. We refine based on a combination of the second spatial derivatives of the density and pressure.

Neutrino-matter interactions that couple neutrino transport to the core-collapse hydrodynamics are computed using the NuLIB library (O’Connor 2015). We consider the same neutrino-matter interactions as O’Connor (2015); Schneider et al. (2019a) and reproduced in Table 3 for completeness. For each EOS table, a consistent set of neutrino opacities is generated using NuLIB. We use 18 logarithmically spaced energy groups, with a highest-energy bin of $\simeq 250 \text{ MeV}$.

3. GR VS. GREP

In the FLASH code, gravity is included in the hydrodynamic equations using an effective gravitational potential,

Table 3. List of neutrino reactions included in simulations. Interactions taken from NuLib (O’Connor 2015) and modeled off of Bruenn (1985); Burrows et al. (2006) with corrections from Horowitz (2002). Interactions with ν are flavor insensitive, while interactions with ν_i are flavor sensitive. ν_x denotes heavy-lepton neutrinos while N denotes a nucleon (either neutron or proton) and A_ZX a specific element with Z protons and mass number A . Thermal processes are included via an effective emissivity (O’Connor 2015).

Production	
Charged-current interactions	Thermal Processes
$\nu_e + n \longleftrightarrow p + e^-$	$e^- + e^+ \longleftrightarrow \nu_x + \bar{\nu}_x$
$\bar{\nu}_e + p \longleftrightarrow n + e^+$	$N + N \longleftrightarrow N + N$
$\nu_e + {}^A_ZX \longleftrightarrow e^- + {}^A_{Z+1}X$	$+ \nu_x + \bar{\nu}_x$
Scattering	
Iso-energetic scattering	Inelastic Scattering
$\nu + \alpha \longleftrightarrow \nu + \alpha$	$\nu_i + e^- \longleftrightarrow \nu_i' + e^{-'}$
$\nu_i + p \longleftrightarrow \nu_i + p$	
$\nu_i + n \longleftrightarrow \nu_i + n$	
$\nu + {}^A_ZX \longleftrightarrow \nu + {}^A_ZX$	

Φ_{eff} , that approximates general relativistic (GR) effects via the “Case A” formalism of Marek et al. (2006). This formalism has never been rigorously tested in the regime of BH formation and, therefore, we do that here.

After the original proposal by Rampp & Janka (2002), the GREP was improved by Marek et al. (2006) who tested several empirical modifications to the standard TOV potential in order to find one that reduced discrepancies in the early evolution of a $15 M_\odot$ progenitor model of Woosley & Weaver (1995) when compared to full GR calculations with the CoCoNuT (Dimmelmeier et al. 2002a,b, 2005) and the AGILE-BOLTZTRAN codes (Liebendörfer et al. 2001, 2002, 2004, 2005). For the simulated collapse, Marek et al. (2006) found that the best suited modification was their “Case A”, where a factor of Γ was introduced in the integrand of the TOV mass equation. The “Case A” GREP equations are given here for reference,

$$\Phi_{\text{eff}}(r) = -4\pi G \int_0^r \left(\frac{m_{\text{TOV}}}{4\pi} + r'^3(P + p_\nu)/c^2 \right) \times \frac{1}{\Gamma^2} \left(\frac{\rho + (e + P)/c^2}{\rho} \right) \frac{dr'}{r'^2}. \quad (3)$$

Here, P is the matter pressure, p_ν is the neutrino pressure, ρ is the rest-mass density, e is the internal energy density, and c is the speed of light. The effective TOV mass is given by,

$$m_{\text{TOV}}(r) = 4\pi \int_0^r r'^2 \left(\rho + (e + E + \frac{vF}{c^2\Gamma})/c^2 \right) \times \Gamma dr', \quad (4)$$

where E is the neutrino energy density, v is the fluid velocity, F is the neutrino flux, and the metric function Γ is given by

$$\Gamma = \sqrt{1 + \left(\frac{v}{c}\right)^2 - \frac{2Gm_{\text{TOV}}}{c^2 r'}}. \quad (5)$$

In Equation (4), we highlight in bold the additional factor of Γ which is not present in the standard TOV equations. In what follows, we ignore the term proportional to vF as its contribution to core-collapse dynamics is negligible, $vF \ll E$.

This change, as motivated by Marek et al. (2006), reduces the TOV mass, m_{TOV} , in the potential, since $\Gamma < 1$. This compensates for the lack of distinction between the proper volume and the coordinate volume that acts to overestimate m_{TOV} . The “Case A” effective potential is used throughout the literature for including effective general relativistic gravity in Newtonian hydrodynamic simulations. This includes several BH formation studies (Hüdepohl 2014; Pan et al. 2018; Walk et al. 2019). While there has been comparisons to published literature simulations in select cases (Hüdepohl 2014; O’Connor et al. 2018), the “Case A” effective potential has never been systematically tested against fully general relativistic simulations for BH formation. Since we focus on BH formation, in this section we systematically compare core-collapse evolutions for many progenitors from Sukhbold et al. (2018)¹ with different compactnesses using the general-relativistic radiation-hydrodynamics code GR1D (O’Connor & Ott 2010; O’Connor 2015) and the FLASH code using the modified TOV effective potential. In the GR1D runs we use the same baseline EOS (Section 2.2) and the same NuLib table generated with parameters described in Section 2.3. The computational grid in GR1D is set to have 700 grid cells, constant cell size of 200 m out to a radius of 20 km, and then geometrically increasing cell size to an outer radius where the baryonic density is $2 \times 10^3 \text{ g cm}^{-3}$. In order to match the initial setup used in FLASH we map stellar mass rest-mass density ρ , proton fraction y_p , and temperature T from the progenitor star to GR1D. To evolve stably until late times in GR1D, we neglect velocity terms and inelastic scattering in this set of comparison runs in both GR1D and FLASH. For the purposes of testing the effective potential this approximation is justified.

In Figure 3, we compare the central density of core-collapse simulations performed using GR1D to FLASH simulations using the “Case A” effective potential for 8 progenitor models that span a wide range of compactness. This evolution agrees quite well in the early times after core bounce, $t - t_{\text{bounce}} \lesssim 0.1 \text{ s}$. The “Case A” effective potential slightly overestimates the central density at intermediate times, $0.1 \text{ s} \lesssim t - t_{\text{bounce}} \lesssim t_{\text{BH}}$, but we stress that it agrees in many other quantities quite well. These include the neutrino luminosity, neutrino average energies, and shock

¹ We choose the model set with reduced mass loss (by a factor of 10), which results in particularly compact supernova progenitors.

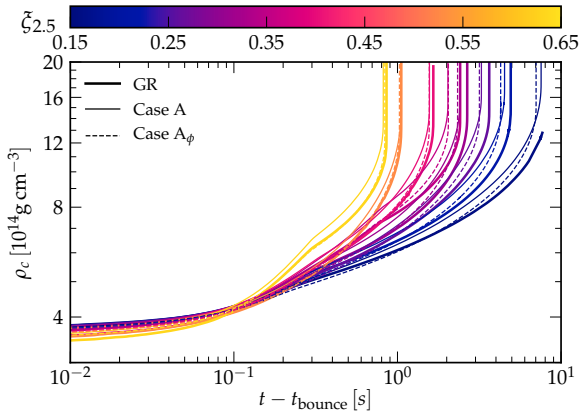


Figure 3. Comparison of central density evolution for full GR simulations using GR1D and two different GREP approximations using FLASH, see text. We limit the plot to 8 pre-SN progenitor models that span a wide range in compactnesses for clarity and stress that all other models behave similarly. Soon after bounce, $t - t_{\text{bounce}} \lesssim 0.1$ s, all approaches predict quite similar evolutions. At later times, $0.1 \text{ s} \lesssim t - t_{\text{bounce}} \lesssim t_{\text{BH}}$, the “Case A” effective potential predicts slightly higher central density than the full GR and the “Case A $_{\phi}$ ” effective potential, the latter two agreeing quite well. Near BH formation the density evolution becomes quite similar again, especially for more compact pre-SN progenitors.

radius evolution (Granqvist 2019). Near the time of BH formation the central densities generally converge again in the two cases, especially for the most compact progenitors.

We also explore an additional case, which we call “Case A $_{\phi}$ ”. Here, we add the additional factor of Γ to the gravitational potential instead of the TOV mass. The central density evolution agrees remarkably well with the full GR case, especially early on and for the most compact progenitors. However, most other quantities, like the emergent neutrino luminosities, tend to show greater deviations from the full GR results when compared to the “Case A” method (Granqvist 2019). Therefore we choose to continue to use the “Case A” potential and do not advocate for our new “Case A $_{\phi}$ ”.

In Figure 3, we show that the BH formation time, t_{BH} , for each pre-SN progenitor is very similar for simulations that use full GR and the two different GREP approaches. This is in agreement with the results of Couch et al. (2019) for comparisons between full GR simulations and the “Case A” GREP approximation using FLASH. However, as we show in Figure 4 for 15 chosen pre-SN progenitors from Sukhbold et al. (2018), full GR simulations consistently take longer to collapse than their GREP counterparts. Also, “Case A $_{\phi}$ ”, despite predicting a more accurate PNS central density evolution than the “Case A” approach, often underestimates the BH formation time by a slightly larger margin than “Case A”. For the progenitors where GR1D runs reached BH formation, in most cases they took 3% to 8% (8% to 16%) more time after core bounce than did the FLASH GREP runs for progenitors with $\xi_{2.5} \gtrsim 0.4$ ($\xi_{2.5} \lesssim 0.4$). For a more indepth

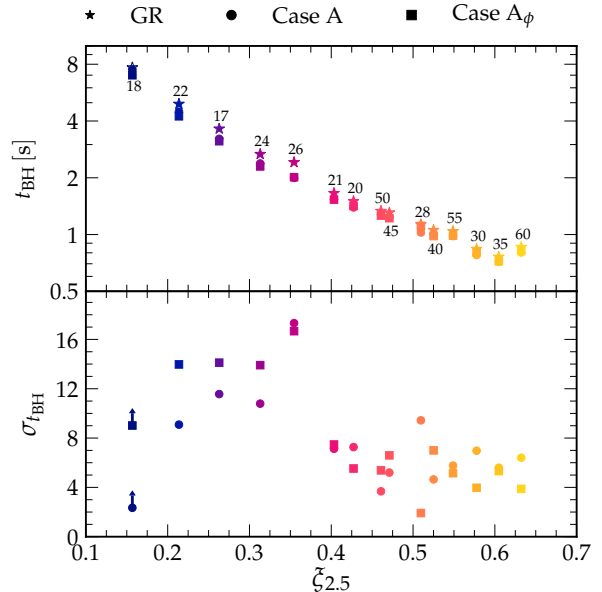


Figure 4. Comparison of the BH formation time for full GR simulations using GR1D and the “Case A” and “Case A $_{\phi}$ ” GREP approximations using FLASH. We limit the plot to 15 pre-SN progenitor models that span a wide range in compactnesses for clarity. Symbols are colored according to their compactness, as in Fig. 3, and we also write explicitly the ZAMS mass of the progenitors in M_{\odot} on the top plot. For the $18 M_{\odot}$ run, where the GR simulation did not reach BH formation due to its increasing computational cost, we replaced the \star symbol by a \star symbol to denote the maximum simulation run time (see also Fig. 3). GR simulations that formed a BH took, on average, 4 to 8% longer to do so than their GREP counterparts for the more compact progenitors and 8 to 16% longer for the less compact ones.

analysis, although with a different EOS, we refer the reader to Granqvist (2019).

4. RESULTS

We start our analysis detailing how pre-SN progenitor structure affects its core-collapse evolution until BH formation. First, we examine two extreme pre-SN progenitor cases, the high compactness progenitor u75WHW02 ($\xi_{2.5} = 0.88$) and the low compactness progenitor s50WH07 ($\xi_{2.5} = 0.22$). Using our baseline EOS we find, as expected, that the compact model collapses to a BH rather quickly, 447 ms after core bounce for u75WHW02, and takes a relatively long time to collapse for the low compactness progenitor, 4478 ms after core bounce for s50WH07.

4.1. High compactness pre-supernova progenitor

In Figure 5 we show the post bounce evolution of the u75WHW02 progenitor star simulated using our baseline EOS. Evolution is shown until 1 ms before BH formation at $t - t_{\text{bounce}} = 447$ ms, defined as the time where the core density surpasses $2.0 \times 10^{15} \text{ g cm}^{-3}$. At core bounce, the central density and temperature are approximately $1.5 n_{\text{sat}}$ and

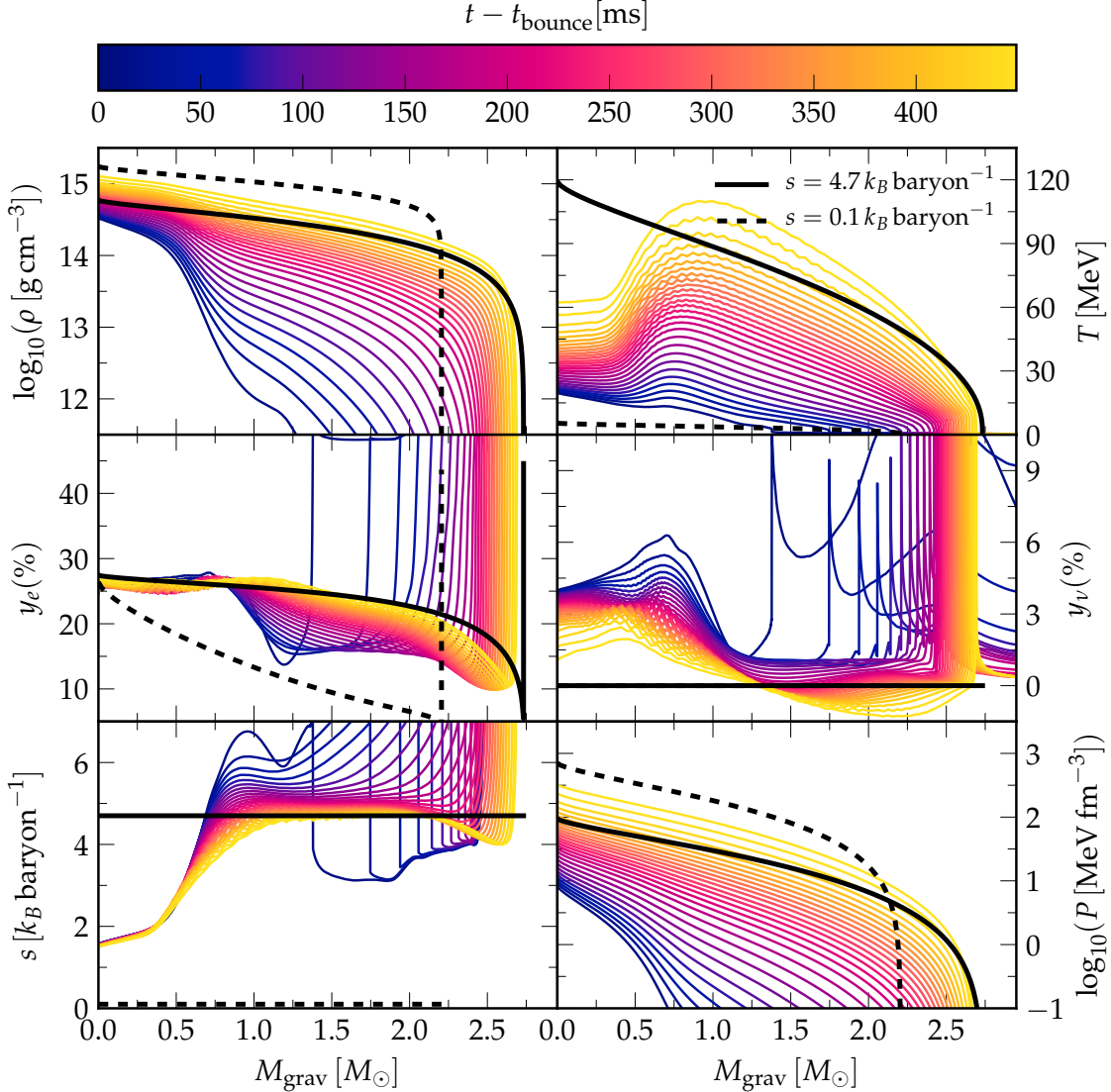


Figure 5. Time evolution from core bounce to BH formation ($t - t_{\text{bounce}} = 447$ ms) of the pre-SN u75WHW02 model of Woosley et al. (2002). We plot the baryonic mass density ρ (top left), temperature T (top right), lepton fraction $y_e = (n_{e^-} - n_{e^+})/n$ (center left, equal to the proton fraction $y_e = y_p = n_p/n$), neutrino number fraction (center right, $y_\nu = (n_\nu - n_{\bar{\nu}})/n$), entropy s (bottom left), and pressure P as a function of gravitational mass coordinate M_{grav} , i.e. Equation (4). Additionally, we plot the properties of a cold ($s = 0.1 k_B \text{ baryon}^{-1}$) and a hot ($s = 4.7 k_B \text{ baryon}^{-1}$) non-rotating beta-equilibrated ($y_\nu = 0$) NS.

20 MeV, respectively. After bounce the core compresses quickly, baryon number density increases almost one order of magnitude in less than 500 ms, and its temperature rises above 50 MeV. Despite increasing density and temperature throughout the PNS, entropy and proton fraction below mass coordinate $M_{\text{grav}} \simeq 0.7 M_\odot$ barely change. Meanwhile, due to the high compactness of this progenitor ($\xi_{2.5} = 0.88$), over $1 M_\odot$ is accreted onto the PNS within a few hundred milliseconds of core bounce. Fast accretion quickly heats up the outer layers of the PNS to temperatures of $\mathcal{O}(10 \text{ MeV})$ and intermediate layers to $\mathcal{O}(100 \text{ MeV})$. Some of the heat diffuses inwards but this is relatively limited (as compared to the lower compactness model) due to the very rapid post-bounce evolution. At the time of BH formation,

the temperature peaks at mass coordinate $M_{\text{grav}} \simeq 0.9 M_\odot$. Neutrino and anti-neutrino emission processes and their diffusion move matter towards beta-equilibrium and decrease the average entropy of the PNS, rendering it almost uniform at $s \simeq 4.7 k_B \text{ baryon}^{-1}$ by BH formation time between mass coordinates $1.0 \lesssim M_{\text{grav}}/M_\odot \lesssim 2.0$.

We compare the evolution of the collapsing star to the most massive beta-equilibrated NS possible. The comparison is made for two cases: (1) a PNS with constant entropy $s = 0.1 k_B \text{ baryon}^{-1}$, which serves as a proxy for a cold NS, and (2) for a hot NS with constant entropy $s = \bar{s}(t_{\text{BH}})$. Here, $\bar{s}(t)$ is the most common entropy value at a given time t defined as

$$\bar{s}(t) = \max(\{M_s(t)\}), \quad (6)$$

where

$$M_s(t) = \int_0^{M^{\text{PNS}}} [H(s(M) - 0.01) - H(s(M) + 0.01)] dM, \quad (7)$$

with H the Heaviside step function, $s(M)$ the entropy at mass coordinate M in units of $k_B \text{ baryon}^{-1}$ and M^{PNS} the mass enclosed by the PNS, *i.e.*, the mass within the region with density larger than $10^{11} \text{ g cm}^{-3}$. We find that this definition displays a smoother and more stable evolution than the maximum entropy inside the PNS within a mass or density coordinate. Moreover, we see only small difference between choosing the gravitational or the baryonic mass for the computation in Equation (6). For the progenitor and EOS discussed in this section we find that $\tilde{s}(t_{\text{BH}}) = 4.7 k_B \text{ baryon}^{-1}$.

We observe that collapse to a BH occurs when the total *gravitational* mass of the PNS, $M_{\text{grav}}^{\text{PNS}}$, is within 1% of $M_{\text{grav}}^{\text{max},\tilde{s}}$, the maximum mass supported by a hot NS with constant entropy $\tilde{s}(t_{\text{BH}})$. Here, and in what follows, a M with a numeric superscript indicates the mass of a constant entropy star with the superscript denoting the entropy in units of $k_B \text{ baryon}^{-1}$. We note that approximately 300 ms after bounce, both the baryonic and gravitational masses of the PNS are already a few tenths of a solar mass larger than the maximum masses supported by a cold non-rotating beta-equilibrated NS. As there is no mechanism for the PNS to lose baryonic mass the collapse into a BH is inevitable even if accretion were abruptly cutoff and neutrinos had enough time to carry away all of the mass associated with the excess thermal energy.

4.2. Low compactness pre-supernova progenitor

In Figure 6, we plot the evolution of the s50WH07 progenitor using our baseline EOS. Due to its relatively low compactness, this progenitor star's structure leads to a much lower accretion rate than the u75WHW02 progenitor and, therefore, has a much longer time to equilibrate between core bounce and the collapse to a BH at $t - t_{\text{bounce}} = 4478 \text{ ms}$. Except for the inner and outermost layers of the star, enough neutrinos have been emitted that most of the PNS is close to beta-equilibrium ($y_\nu = 0$) by the end of the simulation. Thus, heat from the accreted layers has had time to diffuse inwards towards the PNS center and its entropy to decrease to $\tilde{s} \simeq 2.7 k_B \text{ baryon}^{-1}$ between mass coordinates $0.5 \lesssim M_{\text{grav}}/M_\odot \lesssim 2.0$ at the point of BH formation. Compared to the maximum mass of a hot non-rotating beta-equilibrated NS with constant entropy $\tilde{s} = 2.7 k_B \text{ baryon}^{-1}$, we observe that the PNS gravitational mass, $M_{\text{grav}}^{\text{PNS}} = 2.30 M_\odot$ is only slightly above the maximum gravitational mass supported by the hot star with constant entropy $2.7 k_B \text{ baryon}^{-1}$, $M_{\text{grav}}^{\text{max},2.7} = 2.29 M_\odot$. Also, collapse to a BH takes place even though the PNS baryonic mass $M_{\text{baryon}}^{\text{PNS}} = 2.55 M_\odot$ is below the limit $M_{\text{baryon}}^{\text{max},2.7} = 2.60 M_\odot$. Furthermore, even this maximum baryonic mass

supported for a hot NS with $\tilde{s} = 2.7 k_B \text{ baryon}^{-1}$ is below that of a cold non-rotating beta-equilibrated NS, *i.e.*, $M_{\text{baryon}}^{\text{max},2.7} < M_{\text{baryon}}^{\text{max},0} = 2.65 M_\odot$. This implies that there is an intricate interplay between accretion, which increases the total baryonic and gravitational mass of the PNS and pushes it towards collapse into a BH, and neutrino emission, which decreases the gravitational mass of the PNS and can help revive the shock to prevent the gravitational instability that leads to BH formation. In the simulation of the u75WHW02 progenitor, the PNS collapses into a BH happens once its *gravitational* mass exceeds 99% of $M_{\text{grav}}^{\text{max},\tilde{s}}$, while in the case of the s50WH07 progenitor the PNS *gravitational* mass slightly exceeds $M_{\text{grav}}^{\text{max},\tilde{s}}$. The difference is due to the contribution of the relatively colder core of the PNS formed from the core collapse of the u75WHW02 progenitor, which cannot support as much pressure before BH formation.

In Figure 7, we show the evolution of the PNS baryonic and gravitational masses, $M_{\text{baryon}}^{\text{PNS}}$ and $M_{\text{grav}}^{\text{PNS}}$, respectively, with respect to the most common PNS entropy, \tilde{s} , see Equation (6), and the PNS mass averaged entropy

$$\bar{s} = \frac{1}{M^{\text{PNS}}} \int_0^{M^{\text{PNS}}} s(M) dM \quad (8)$$

We plot curves for the six pre-SN progenitor models chosen from Woosley et al. (2002) and Woosley & Heger (2007), see Table 1, and simulated using our baseline EOS. We also include the maximum supported baryonic and gravitational masses for hot stars with a constant entropy s , $M^{\text{max},s}$, for the baseline EOS used in the simulations. The plot with respect to the gravitational mass reinforces the idea that, for a given progenitor and, as we will show later, a given EOS, BH formation occurs only once $M_{\text{grav}}^{\text{PNS}} \gtrsim M_{\text{grav}}^{\text{max},\tilde{s}}$. Meanwhile, the plot showing the evolution of the PNS baryonic mass emphasizes that (1) BH formation correlates with excess gravitational mass and not baryonic mass and (2) that collapse into a BH can happen for PNSs with baryonic masses lower than the maximum supported by a cold NS.

For both progenitors described here in detail, u75WHW02 and s50WH07, our qualitative results for the PNS profile evolution in the first seconds after core bounce are in broad agreement with other PNS evolution simulations in spherical symmetry (Sumiyoshi et al. 2005, 2007, 2008, 2009; Martínez-Pinedo et al. 2012; Roberts et al. 2012; Roberts & Reddy 2016; Fischer et al. 2009, 2010, 2012; Nakazato et al. 2012, 2013, 2018; Nakazato & Suzuki 2019; Banik et al. 2014; Char et al. 2015). While some of these studies focused on the PNS path towards BH formation and EOS effects, many were only interested in long term evolutions of PNSs that would eventually form a cold NS. Fischer et al. (2010, 2012); Martínez-Pinedo et al. (2012) simulated core collapse and PNS evolution for several seconds for pre-SN progenitor stars of 8.8, 10.8, 15, and 18 M_\odot . In these works, explosions were achieved by artificially enhancing the electronic charged current reaction rates except for the lightest progenitor, which is able to explode even in spherically

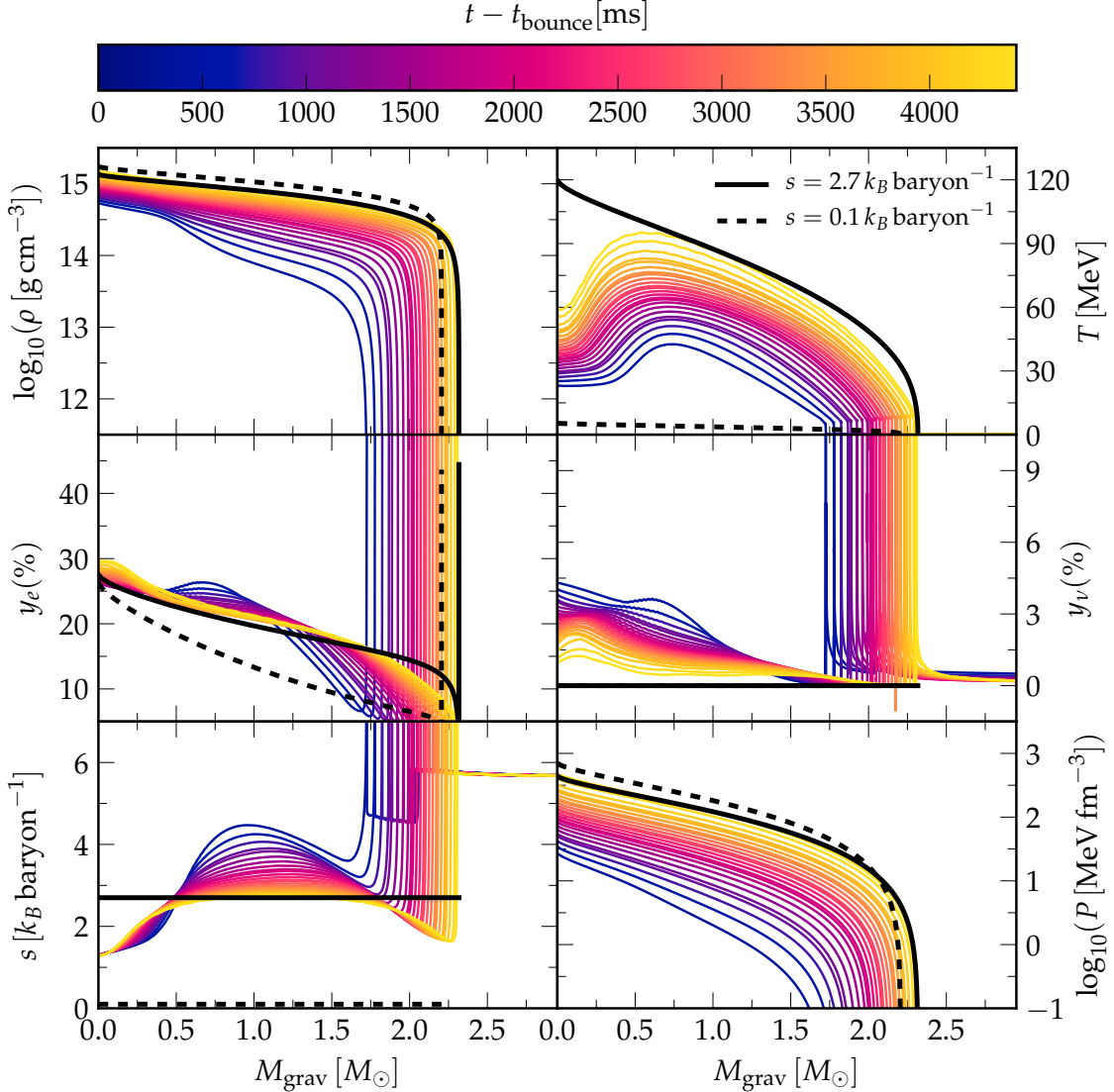


Figure 6. Time evolution from core bounce to BH formation ($t - t_{\text{bounce}} = 4478$ ms) of the pre-SN s50WH07 model of Woosley & Heger (2007). Plot order as in Figure 5. Additionally, we plot the properties of a cold ($s = 0.1 k_B \text{ baryon}^{-1}$) and a hot ($s = 2.7 k_B \text{ baryon}^{-1}$) non-rotating beta-equilibrated ($y_\nu = 0$) NS.

symmetric simulations. Nakazato et al. (2013) simulated PNS cooling for eight massive progenitor models using the H. Shen EOS (Shen et al. 1998a,b) for up to 20 seconds after core bounce by removing the stellar mantle above the shock region after 100, 200, and 300 ms after core bounce. In the one case where Nakazato et al. (2013) did not remove the outer layers of the star after core bounce, for a $30 M_\odot$ progenitor with $Z = 0.004$ metallicity, the PNS collapsed into a BH within 842 ms and a gravitational mass $M_{\text{grav}}^{\text{PNS}} \simeq 2.53 M_\odot$ assuming all the binding energy was radiated away in neutrinos. Nakazato et al. (2018); Nakazato & Suzuki (2019) evolved PNSs for up to 80 seconds after removing the regions above the shock 300 ms after core bounce to study the effect of the EOS in the cooling timescales. Meanwhile, Roberts & Reddy (2016) excised the inner $1.42 M_\odot$ of the PNS and evolved it for 100 seconds using the LS₂₂₀

EOS of Lattimer & Swesty (1991). Unlike these previous PNS evolution studies, however, we do not force explosions to occur. Instead, we allow for the overlying material above the PNS to continue to accrete, as expected in spherically symmetric simulations, and drive BH formation. We also do not model convective instabilities that arise within the PNS and drive convection and turbulence, even though those are sensitive to the EOS (Roberts 2012) and render the entropy profile within the PNS monotonically increasing (Dessart et al. 2006; Roberts 2012; Pan et al. 2018; Gossan et al. 2019). Note that this would remove the negative entropy gradients seen between $2.1 M_\odot \lesssim M_{\text{grav}}^{\text{PNS}} \lesssim 2.6 M_\odot$ ($1.7 M_\odot \lesssim M_{\text{grav}}^{\text{PNS}} \lesssim 2.3 M_\odot$) for the u75WHW02 (s50WH07) progenitor and may affect each combination of progenitor and EOS in a unique manner. Thus, a natural follow up to our work is a similar multidimensional study. An analysis of the results of

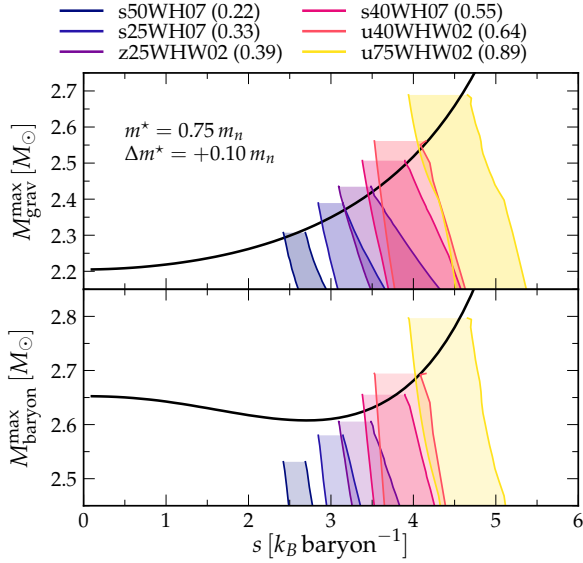


Figure 7. Evolution of the gravitational (top) and baryonic (bottom) masses during the core-collapse of the six pre-SN progenitor models chosen from Woosley et al. (2002) and Woosley & Heger (2007). Shaded areas are bound left by the mass weighted average entropy \bar{s} , Equation (8), right by the most common entropy \tilde{s} within the PNS, Equation (6), and top by the PNS mass at BH formation time. Black lines are the maximum possible mass $M^{\max,s}$ obtained solving the TOV equations for a NS with constant entropy s for our baseline EOS (Section 2). Collapse to a BH takes place, to a very good approximation, once the *gravitational* mass of the PNS exceeds the maximum gravitational mass supported by a hot NS with entropy equal to the most common entropy (i.e. $s = \tilde{s}(t_{\text{BH}})$ inside the PNS.)

Sumiyoshi et al. (2006, 2007, 2008, 2009); Fischer et al. (2009); O’Connor & Ott (2011); Nakazato et al. (2012); Hempel et al. (2012); Steiner et al. (2013); Banik et al. (2014); Char et al. (2015); Pan et al. (2018) in light of our conclusions are discussed in detail at the end of this section.

4.3. Multiple progenitors

We now explore the relationship between collapse to BH and gravitational mass of the PNS for 45 pre-SN progenitors of Sukhbold et al. (2018), Section 2.1. Again, we simulate all core collapses until BH formation occurs. In Figure 8, we plot the central density for each progenitor and observe, as expected, that the time for a BH to form decreases with increasing compactness (O’Connor & Ott 2011). The BH formation time is the time it takes to accrete the critical mass element that has a baryonic mass coordinate equal to the PNS baryonic mass at the point of BH formation. This occurs approximately at (Burrows 1986; O’Connor & Ott 2011)

$$t_{\text{BH}} \simeq t_{\text{ff}}^{M_{\text{BH}}} = A \xi_{2.5}^{-b} s. \quad (9)$$

where $M_{\text{BH}} = M_{\text{PNS}}(t_{\text{BH}})$ and $t_{\text{ff}}^{M_{\text{BH}}}$ is the free-fall time at mass coordinate M_{BH} . For realistic EOSs and progeni-

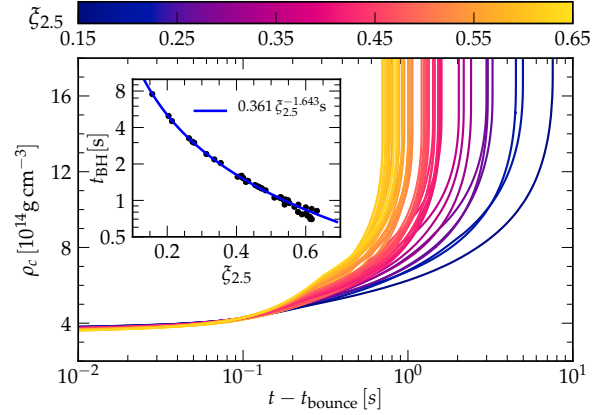


Figure 8. Evolution of the central density ρ_c as a function of post bounce time $t - t_{\text{bounce}}$ for the 45 pre-SN progenitors of Sukhbold et al. (2018). In the inset we plot the BH formation time t_{BH} as a function of the compactness $\xi_{2.5}$, Equation (1) and its best fitting curve, Equation (9).

tors $M_{\text{PNS}}(t_{\text{BH}}) \simeq 2.0 - 3.0 M_{\odot}$ and, thus, setting $M_{\text{BH}} = 2.5 M_{\odot}$ is a reasonable approximation. A straightforward calculation of $t_{\text{ff}}^{2.5 M_{\odot}}$ leads to $A = 0.241$ and $b = 3/2$ (O’Connor & Ott 2011). For our baseline EOS and the progenitors of Sukhbold et al. (2018) discussed here which collapse into a BH we have $A = 0.361 \pm 0.004$ and $b = 1.643 \pm 0.008$. Meanwhile, for the six progenitors of Woosley et al. (2002) and Woosley & Heger (2007), see Table 1, we obtain $A = 0.332 \pm 0.011$ and $b = 1.728 \pm 0.024$. We observe that the exponents b and amplitudes A are both larger for the simulated collapses than the values obtained from the Newtonian free-fall time (Burrows 1986; O’Connor & Ott 2011; Couch et al. 2019). These are due to the free-fall time not accounting for existent pressure support for the infalling mass element, which depends on details of the progenitor structure and the arbitrary initial reference time, here set to be the PNS bounce time. Differences between the fitting for the two progenitor sets are not significant, 5% for the exponent and 9% for the amplitude, given that they sample the range of compactnesses at different frequencies and that one set includes only six progenitor stars.

In Figure 9, we plot the PNS gravitational mass, $M_{\text{grav}}^{\text{PNS}}$, accretion rates, \dot{M} ; and the evolution of PNS and shock radii, R_{PNS} and R_{shock} , respectively. During the first $\simeq 200$ ms post core-bounce, progenitors with higher compactness form, in general, PNSs with larger radii. The behavior changes at later times since accretion rates increase with compactness which, in turn, result in higher pressures on top of the PNS and force the PNS to contract faster. This would have implications for GW emission as the more compact and more massive a PNS is the stronger the gravitational waves and the higher the frequencies it emits (Pan et al. 2018; Morozova et al. 2018; Torres-Forné et al. 2019).

Similar to the PNS radii, the shock radii also follow a somewhat well defined trend for all progenitors. The exceptions occur near the times when the shock crosses steep den-

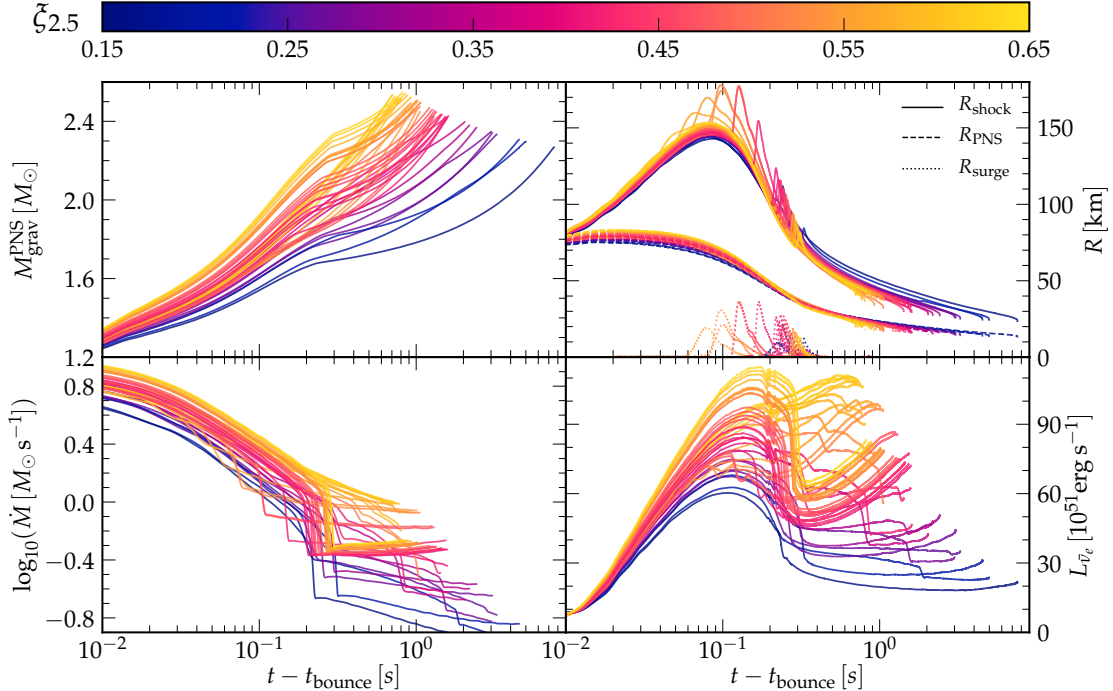


Figure 9. Evolution of the PNS gravitational mass $M_{\text{grav}}^{\text{PNS}}$ (top left), accretion rate \dot{M} (bottom left), shock R_{shock} , shock surge R_{surge} , and PNS radii R_{PNS} (top right), and electron anti-neutrino luminosity $L_{\bar{\nu}_e}$ (bottom right) for core-collapse simulations of 45 pre-SN progenitor models of [Sukhbold et al. \(2018\)](#), see Section 2.1. We estimated the gravitational mass by computing the baryonic mass of the PNS (defined by $\rho > 10^{11} \text{ g cm}^{-3}$) and subtracting the total integrated luminosity of the emitted neutrinos. Large declines in accretion rates that occur due to sharp density drops in the progenitor models (see Figure 1) cause shock radii to expand further than expected from a smooth accretion rate, shown as R_{surge} in the top right plot. See discussion in text. Note that not all progenitors show sharp declines in accretion rate. Neutrino luminosities, represented here by the electron anti-neutrino, also show behavior that depends on the progenitor profile.

sity gradients, such as the interface between the Si and Si-O shell, and accretion rates drop dramatically. Lower accretion allows shock radii, if not already increasing fast due to early post-bounce dynamics, to expand significantly. At such times when the shock radius crosses a shell boundary, which takes place between 40 ms and 400 ms after bounce for most progenitors where this occurs, the shock radii quickly expands an extra $10 \text{ km} \lesssim R_{\text{surge}} \lesssim 30 \text{ km}$, but recedes soon after. This outcome is expected for spherically symmetric simulations of core collapse. However, in multidimensional simulations the accretion of the interface at the boundary between the Si and Si-O shell is often the driver of a successful SN ([Summa et al. 2016, 2018](#); [Ott et al. 2018](#); [Vartanyan et al. 2019](#)).

For most pre-SN progenitors, including the ones considered here, the Si/Si-O interface crosses the region where the entropy is $s = 4 k_B \text{ baryon}^{-1}$. This interface also coincides with the steepest density and entropy gradients throughout the star and occurs near mass coordinate $M \simeq 2 M_{\odot}$, which is discernible as a large density drop in the stellar profile, see Figure 1. Considering this, [Ertl et al. \(2016\)](#) were able to correlate successful supernovae explosions with the mass coordinate $M(s = 4 k_B \text{ baryon}^{-1})$ and how steep the entropy gradient $\mu_4 = dm/dr|_{s=4 k_B \text{ baryon}^{-1}}$ is at such location. This is because M_4 is related to when the sudden drop in ac-

cretion rate occurs while μ_4 determines how significant the drop is. If the drop in accretion rate is close to when neutrino luminosity is at a maximum an explosion sets in ([Ertl et al. 2016](#)).

We estimate the surge in shock radii caused by the shock radius crossing a steep density/entropy gradient in our simulations, R_{surge} in Figure 9. R_{surge} is computed by subtracting a smoothed shock radius from R_{shock} . The smoothed shock radius is a fit to R_{shock} that excludes data points near where accretion rate drops significantly². We observe that R_{surge} is larger if the shock crosses a boundary layer near when neutrino luminosity is close to a maximum in its trend, $t - t_{\text{bounce}} \simeq 80 - 200 \text{ ms}$. Thus, as in [Ertl et al. \(2016\)](#), we expect larger R_{surge} to correlate with successful supernovae explosions in multidimensional simulations. We reiterate that these radii surges do not correlate with compactness of the pre-SN progenitor, but with the location and density gradient of the advected boundary layer.

Finally, we also show in Figure 9 the luminosity, $L_{\bar{\nu}_e}$, of electron anti-neutrinos as their count rate could be the main

² The fit is performed with the `InterpolatedUnivariateSpline` Python module ([Jones et al. 2001](#)) excluding R_{shock} in the region where $d \log \dot{M} / d \log(t) < -2$ and up to $\simeq 100 \text{ ms}$ afterwards

observable informing us of progenitor structure and possible PNS collapse to a BH during a galactic core-collapse (Scholberg 2012). In the earlier stages of collapse, electron anti-neutrino luminosity rises quickly and peaks approximately 100 to 150 ms after core bounce. For pre-SN progenitors where accretion rates drop abruptly due to the advection of a boundary shell, so do the neutrino luminosities as it is accretion that fuels the neutrino production. Thus, while the BH formation time is well correlated with the pre-SN progenitor compactness, the behavior of most other observables after the first ~ 200 ms, such as neutrino luminosity, shock radius, and accretion rate, is not well determined solely by progenitor compactness ξ_M , but also depend on pre-SN progenitor structure (Buras et al. 2006; O’Connor & Ott 2013; Ertl et al. 2016; Ebinger et al. 2018). Finally, the neutrino signal is abruptly cut-off at the moment of BH formation due to the neutrinosphere being inside the BH event horizon (Sumiyoshi et al. 2006), although we are not able to evolve our simulations until this happens.

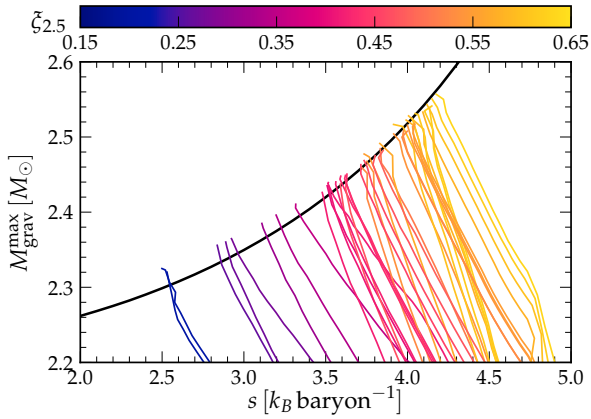


Figure 10. Evolution of the most common entropy (\bar{s}) inside the PNS and its gravitational mass for the progenitors of Sukhbold et al. (2018). Curves are compared to the maximum gravitational mass supported by a hot NS with constant entropy. Collapse to a BH happens soon after the gravitational mass of the PNS is above the limit defined by the hot constant-entropy NS.

As for the Woosley et al. (2002) and Woosley & Heger (2007) progenitors, we also consider the entropy evolution of the PNS for the Sukhbold et al. (2018) progenitors. In Figure 10, we plot the gravitational mass of the PNS as a function of the most common entropy, \bar{s} , inside the PNS. We compare these curves for each of the progenitors to the maximum gravitational mass supported by a hot NS with a constant entropy, which is obtained by solving the TOV equations for our baseline EOS. We note that in our TOV solutions we do not include the effects of thermal neutrinos, which are naturally included in our neutrino transport simulations. We have checked that adding these to the TOV solutions for constant entropy NSs changes the maximum gravitational mass by $< 1\%$ for all $s < 4 k_B \text{ baryon}^{-1}$. BH formation occurs, in almost every case, soon after the grav-

itational mass of the PNS is above the limit defined by the constant-entropy NS for our EOS, $M_{\text{grav}}^{\text{max},s}$. Only in a few cases of high-compactness progenitor collapse BH forms with a mass below $M_{\text{grav}}^{\text{max},s}$, but still very close to it.

4.4. Equation of state effects

In the discussion above we focused on the collapse of 51 pre-SN progenitor models simulated using a single EOS. Now we look at the effects of another 48 EOSs (Section 2.2) on the collapse of the six progenitors of Woosley et al. (2002) and Woosley & Heger (2007), Section 2.1.

In Figure 11 we plot the central density of the PNSs after core bounce until BH formation for the collapse of the pre-SN progenitors u75WHW02 and s50WH07 simulated using the EOSs from sets s_M and s_P of Schneider et al. (2019a). Recall that the EOS set s_M is constructed in such a way that the zero temperature component of each EOS is very similar, while their temperature dependences differ. Set s_P , on the other hand, has the same temperature dependence for all EOSs, while the zero temperature components of their EOSs differ.

For the high compactness progenitor u75WHW02, $\xi_{2.5} = 0.88$, we observe that simulations using set s_M lead to BH formation times that change by almost a factor of 2.5, from $t_{\text{BH}} = 240$ ms for the softest EOS ($m^* = 0.95 m_n$ and $\Delta m^* = 0.30 m_n$) to $t_{\text{BH}} = 592$ ms for the stiffest EOS ($m^* = 0.55 m_n$ and $\Delta m^* = -0.10 m_n$). Meanwhile, for the same progenitor, simulations performed with EOSs in set s_P have BH formation times that differ by at most 15% from each other, $t_{\text{BH}} = 412$ ms for the softest EOS ($P_{\text{SNM}}^{(4)} = 100 \text{ MeV fm}^{-3}$ and $P_{\text{PNM}}^{(4)} = 160 \text{ MeV fm}^{-3}$) and $t_{\text{BH}} = 478$ ms for the stiffest EOS ($P_{\text{SNM}}^{(4)} = 150 \text{ MeV fm}^{-3}$ and $P_{\text{PNM}}^{(4)} = 240 \text{ MeV fm}^{-3}$).

The situation changes for the low compactness progenitor s50WH07, $\xi_{2.5} = 0.22$. In this case, BH formation times for runs simulated using the s_P set extends from $t_{\text{BH}} = 3.5$ s for the softest EOS to almost $t_{\text{BH}} = 5.2$ s for the stiffest EOS, a 48% increase. For set s_M and the same s50WH07 progenitor, however, BH formation times become much less disperse than for the very compact progenitor u75WHW02. Collapse of the PNS into a BH now takes between $t_{\text{BH}} = 3.4$ s for the softest EOS in the set to $t_{\text{BH}} = 4.7$ s for the stiffest, only a 38% difference.

As also shown by Schneider et al. (2019a), the effective mass (m^*) has a higher influence in the collapse evolution than the effective mass splitting (Δm^*). Thus, for a given pre-SN progenitor, clustering of the predicted central densities soon after bounce for EOSs with similar effective masses is expected. Nevertheless, other parameters within their current constraints which were not studied in this work, such as the nuclear incompressibility and symmetry energy at saturation density and its slope, also play a part in setting the central density after core bounce (Steiner et al. 2013; Yasin et al. 2018; Schneider et al. 2019a). As expected, for EOSs that differ only in their pressure at high densities, such

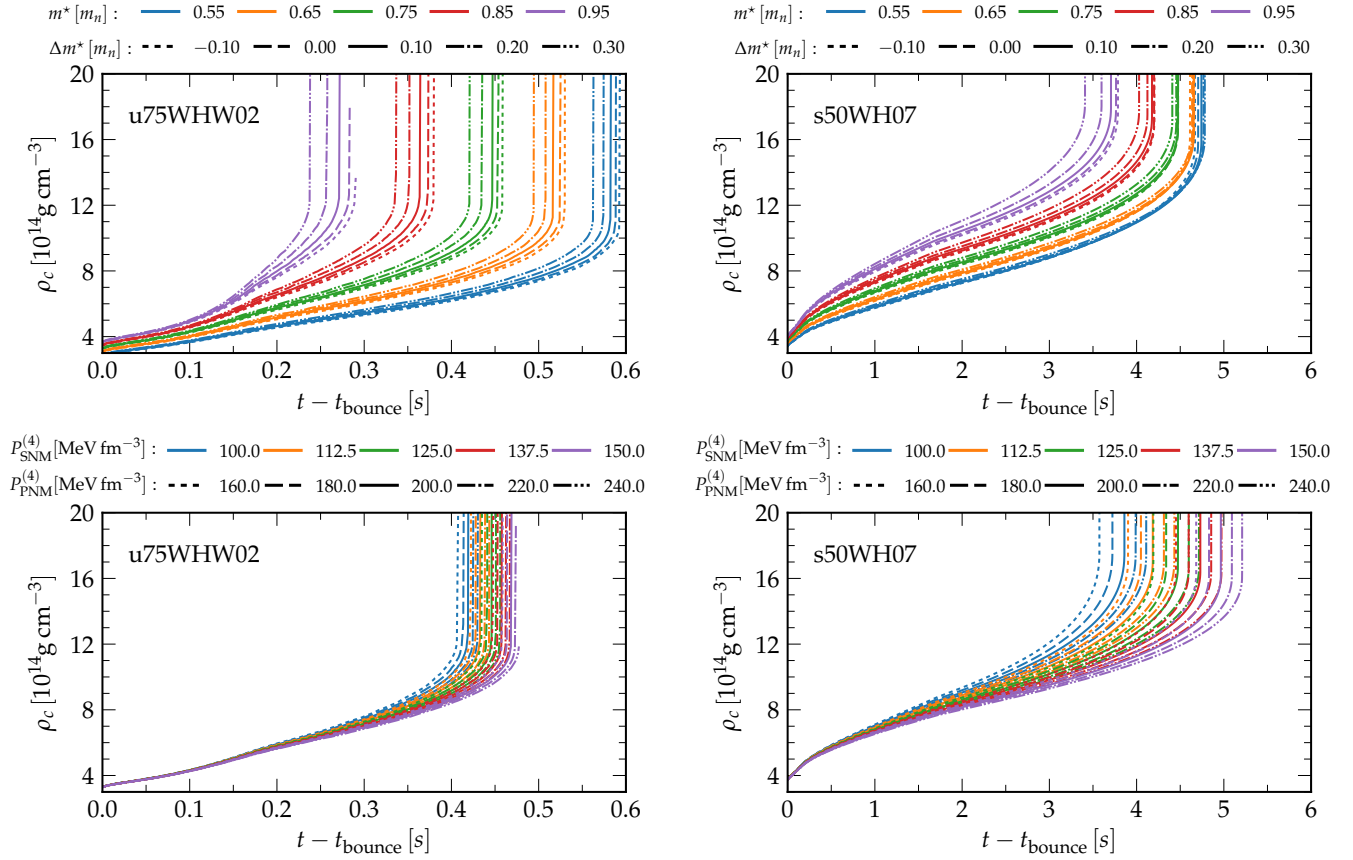


Figure 11. Central density evolution for the u75WHW02 (left) and s50WH07 (right) progenitors, see Section 2.1 for the EOS sets s_M (top) and s_P (bottom), see Section 2.2. Differences in the zero temperature EOS, represented by set s_P , result only in small differences in central density evolution for the fast collapsing progenitor u75WHW02. Meanwhile, differences in the temperature dependence of the EOS, represented by set s_M , result in large differences in central density evolution for the same progenitor. For the less compact and slowly contracting PNS resulting from the collapse of pre-SN progenitor s50WH07 the differences in central density between EOS sets s_M and s_P are not as extreme as for the u75WHW02 progenitor.

as the ones in set s_P , significant changes in the PNS evolution occur solely after central density is above $n \gtrsim 3 n_{\text{sat}}$.

In Figure 7 we showed using the baseline EOS of Schneider et al. (2019a) and the progenitors of Woosley et al. (2002) and Woosley & Heger (2007) that PNS was unstable against collapse into a BH only after the PNS gravitational mass overcame or was very close to $M_{\text{grav}}^{\text{max}, \tilde{s}}$, the maximum gravitational mass supported by a hot NS with constant entropy \tilde{s} , see Equation (6). We verified this result to be true for all combinations of 6 progenitors and 49 EOSs discussed here.

Our approach to determine when a PNS collapses into a BH allows us to identify, for a given pre-SN progenitor, which components of the finite-temperature EOS most significantly impact the core-collapse evolution. In Figure 12, we plot the maximum supported gravitational mass for a hot NS with a constant entropy s , $M_{\text{grav}}^{\text{max}, s}$, for the EOSs in set s_M and s_P . As expected, EOSs in set s_M produce very similar low-entropy stars, $s \lesssim 2 k_B \text{ baryon}^{-1}$, and very different high-entropy stars. This is due to their non-thermal EOS components being alike, while their thermal components are quite different. EOSs in set s_P , on the other hand,

have the opposite behavior due to their identical thermal components, but distinct non-thermal high-density profiles.

Also in Figure 12 we show the Gaussian average and its 95% confidence interval of the core-collapse trajectory in $\tilde{s} - M_{\text{grav}}^{\text{PNS}}$ space³. The average is computed over all EOSs in a given set for each of the pre-SN progenitors. It is remarkable that the path traced in $\tilde{s} - M_{\text{grav}}^{\text{PNS}}$ space for each progenitor is almost independent of the chosen EOS up to the point of BH formation. For clarity we pinpoint the moments where BH formation takes place.

A few other remarks about the PNS evolution are important. First, for a given progenitor, the paths drawn in $\tilde{s} - M_{\text{grav}}^{\text{PNS}}$ space averaged over EOSs are, to first order, close to a straight line, at least in the limited region of parameter space plotted. Second, these lines have similar slopes for

³ The Gaussian Process kernel includes an amplitude factor, white noise with level set to 0.1, and a Matrn component with length scale 2 and smoothness 3/2 (Pedregosa et al. 2011). More details at <https://blog.dominodatalab.com/fitting-gaussian-process-models-python/>

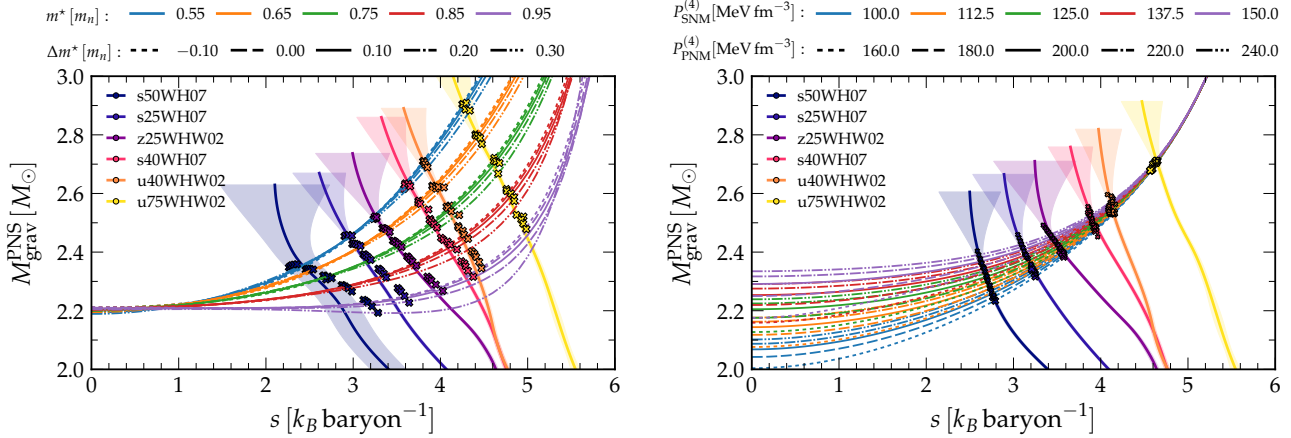


Figure 12. Maximum gravitational mass supported by a hot NS with constant entropy for EOSs in set s_M (left) and s_P (right). Also plotted are the Gaussian averages and their 95% confidence intervals for the core collapse trajectories in $\tilde{s} - M_{\text{grav}}^{\text{PNS}}$ space averaged over all EOSs for each of the six progenitors of Woosley et al. (2002); Woosley & Heger (2007). We extend this curve up to $0.3 M_{\odot}$ beyond the largest mass achieved for a given progenitor. We also pinpoint the moments of BH formation (crosses) of all simulations and note that they deviate little from the Gaussian average curves. We note that the PNS follows a similar trajectory in $\tilde{s} - M_{\text{grav}}^{\text{PNS}}$ for each progenitor, regardless of the EOS, and collapse into a BH occurs shortly after it crosses the maximum gravitational mass threshold supported by a hot NS with constant entropy for the EOS used. The curve for the s50WH07 progenitor and the s_M progenitor set looks like an outlier since some of the points at BH formation time look well outside the average region. This occurs due to the trajectories in $\tilde{s} - M_{\text{grav}}^{\text{PNS}}$ space for the stiffer EOSs in this set having more weight as they take significantly longer to form a BH, as well as the most common entropy, \tilde{s} , for runs with the softer EOSs in the set not decreasing as fast as for the stiffer ones.

all progenitors and, furthermore, are approximately ordered by increasing compactness. Nevertheless, we notice steeper slopes for progenitors that maintain large accretion rates throughout their evolution history. Also, we observe almost no difference between the core-collapse trajectory evolution in $\tilde{s} - M_{\text{grav}}^{\text{PNS}}$ space simulated with EOSs in sets s_M and s_P . The only exception occurs for core-collapse simulations of the s50WH07 pre-SN progenitor, since the slow rate of accretion and distinct thermal component of the EOSs in set s_M allow for different evolution of the PNS entropy near BH formation time. Thus, this is the combination of EOS set and progenitor with the widest confidence level region. All of this, allows us to conclude that for spherically-symmetric core-collapse of compact pre-SN progenitors, the path in $\tilde{s} - M_{\text{grav}}^{\text{PNS}}$ space is almost independent of the EOS. Thus, this trajectory is mainly a function of the pre-SN stellar structure and, to a good approximation, only a function of progenitor compactness. Some of these points can also be inferred from Figure 10 for multiple progenitors and a single EOS. Therefore, we conclude that computing $M_{\text{grav}}^{\text{PNS}}(\tilde{s})$ for a given progenitor for a single EOS may be enough to determine if BH formation would occur faster or slower using a different EOS and what would be the BH initial mass. Such a plot can assist us when making comparisons between different progenitors and a single EOS or between one progenitor and different EOSs. This is discussed next.

The conclusion above can be used to understand the overall behavior displayed by the results shown in Figure 11. A very compact pre-SN progenitors such as u75WHW02, which collapses from a PNS to a BH in a few hundred mil-

liseconds, displays quite a wide (narrow) range of BH formation times when simulated with EOSs in set s_M (s_P). This occurs mainly due to more compact progenitors accreting material fast and not leaving enough time for neutrinos to carry out the excess entropy before gravitational instability settles in. Thus, the path traced by this progenitor in $M_{\text{grav}}^{\text{PNS}} - \tilde{s}$ phase space crosses the maximum supported mass by hot NSs in the high-entropy region, where EOS sets s_M and s_P predict very different scenarios, and lead to very different BH formation times and initial masses. Had we known beforehand the conclusions drawn above, we could have simulated the collapse of u75WHW02 using a single EOS and determined with a reasonable accuracy how long it would take for the PNS to collapse into a BH had we simulated it with any other EOS. Moreover, the initial BH gravitational mass could also have been predicted without performing additional simulations. It is then clear why using EOS set s_M to simulate the collapse of the pre-SN progenitor u75WHW02 leads to quite different BH formation times and initial masses, while for set s_P those times and masses are fairly similar.

Low compactness pre-SN progenitors such as s50WH07 take a few seconds to collapse into a BH due to their much lower accretion rates. Lower accretion rates lead to less compressional heating of the PNS, allowing it more time to emit neutrinos and decrease the total PNS entropy. Due to less thermal support low compactness pre-SN progenitor stars will, for most EOSs, form BHs slower and with lower masses than those resulting from the core collapse of more compact progenitors. From a single simulation of such a

progenitor, using one EOS, we could also determine its path along the $M_{\text{grav}}^{\text{PNS}} - \tilde{s}$ plane, although not as accurately as for more compact progenitors. Yet, it should be reasonably clear now why the initial BH mass and the time it takes for it to form is as diverse for EOS set s_M as it is for set s_P for the s50WH07 progenitor.

4.5. Other EOSs

In Figure 13 we plot the $M_{\text{grav}}^{\text{PNS}}(\tilde{s})$ for many EOSs found in the literature. We plot the baseline SRO EOS used in this study (Schneider et al. 2019a), the APR EOS (Schneider et al. 2019b), the three variants of the Lattimer and Swesty (LS) EOS with incompressibilities $K_{\text{sat}} = 180, 220$ and 375 MeV baryon $^{-1}$ (Lattimer & Swesty 1991), the DD2 and FSU-Gold EOSs (Hempel et al. 2012), the DD2 variant including hyperons BHB $_{\Lambda\phi}$ (Banik 2014), the H. Shen EOS (Shen et al. 1998b) and its variant including Λ hyperons (Shen et al. 2011), the SFHo EOS (Steiner et al. 2013), and the Togashi EOS (Togashi et al. 2017). We also plot the Gaussian averaged trajectory in $M_{\text{grav}}^{\text{PNS}} - \tilde{s}$ space for the six different progenitors discussed in this section for the EOS set s_M . Because the difference in maximum masses $M_{\text{grav}}^{\text{PNS}}(s)$ changes from one EOS to the next for a given entropy s , we expect that BH formation times and their initial masses to also do so. We now use the results of our simulations, which are summarized by the averaged trajectories for each progenitor in $M_{\text{grav}}^{\text{PNS}} - \tilde{s}$ space, see Figure 13, to examine previous works.

First, we note that EOSs that are stiffer at zero entropy/temperature are not necessarily stiffer at finite entropy. In fact, the stiffest EOS at zero temperature, LS $_{375}$, is the softest EOS at $s \simeq 6 k_B$ baryon $^{-1}$. Also, whether an EOS is computed within a relativistic or non-relativistic model matters. Both the Togashi and APR EOSs are computed to reproduce the nuclear potential of Akmal et al. (1998), While Togashi et al. (2017) use a relativistic formalism, Schneider et al. (2019b) use non-relativistic Skyrme-like extension to compute their APR EOS. Although both $M_{\text{grav}}^{\text{max}}(s)$ curves are quite similar, they do not completely agree and the discrepancy between them becomes larger as the entropy increases. In fact, $M_{\text{grav}}^{\text{max}}(s)$ for the APR EOS increases faster than for the Togashi EOS, a result of the non-relativistic formalism allowing very stiff EOSs which lead to superluminal sound speeds at very high densities.

Works by Fischer et al. (2009); Sumiyoshi et al. (2006, 2007) compared BH formation for a few progenitors in simulations that employed the LS $_{180}$ EOS, or the LS $_{220}$ EOS in the case of Sumiyoshi et al. (2008), and the H. Shen EOS (Shen et al. 1998a,b). In all cases these studies found that for a given progenitor the H. Shen EOS predicted PNSs to last longer than the LS $_{180}$ EOS, and, thus, collapsed into BHs with larger initial masses. This is clear from Fig. 13 where the H. Shen EOS always displays a larger maximum PNS mass than both the LS $_{180}$ or LS $_{220}$ EOS.

O'Connor & Ott (2011) studied the EOS dependence of BH formation for over 100 pre-SN progenitors of different compactnesses using the open-source general-relativistic GR1D

code with three-species neutrino leakage and approximate heating scheme (O'Connor & Ott 2010). They compared the core-collapse evolution for four EOSs, three Skyrme-type EOSs from (Lattimer & Swesty 1991) with incompressibilities $K_{\text{sat}} = 180$ MeV (LS $_{180}$), 220 MeV (LS $_{220}$) and 375 MeV (LS $_{375}$) as well as the relativistic mean field (RMF) EOS of Shen et al. (1998a,b) (H. Shen). Although two of these EOSs are excluded by experiments, LS $_{180}$ for being too soft and LS $_{375}$ for being too stiff at zero temperature, they are still useful to understand the EOS dependence of BH formation. With these four EOSs, O'Connor & Ott (2011) observed, amongst other things, that BH formation times and initial masses were similar for the pairs LS $_{180}$ -LS $_{220}$ and LS $_{375}$ -H. Shen EOSs, see their Table 2 and Figure 7. While the LS $_{180}$ and LS $_{220}$ EOSs forecast that BHs will form once the PNS gravitational mass exceeds $\simeq 2.0 M_{\odot}$ for the less compact progenitors and $\simeq 2.5 M_{\odot}$ for the most compact ones, both the H. Shen and LS $_{375}$ EOSs predict that BHs form with initially larger masses, $\simeq 2.5$ – $2.8 M_{\odot}$. Additionally, the differences in initial mass and collapse times between the EOS pairs, LS $_{180}$ -LS $_{220}$ and LS $_{375}$ -H. Shen, decrease with increasing progenitor compactness. Furthermore, LS $_{375}$ was the only EOS to allow BH formation to take place for PNS gravitational masses lower than the maximum supported by the EOS at zero temperature.

All of the observations by O'Connor & Ott (2011) described above can be understood from Figure 13. First, we see that for hot NSs with constant entropy s , the LS $_{180}$ and LS $_{220}$ EOSs predict maximum hot-NS gravitational masses that differ by approximately $0.2 M_{\odot}$ for $s \lesssim 3 k_B$ baryon $^{-1}$. This difference in the maximum gravitational mass decreases for higher entropy and inverts for $s > 5.1 k_B$ baryon $^{-1}$. Thus, for spherically symmetric CCSN simulations using these two EOSs, BHs will form soon after the PNS overcomes a mass of $\simeq 1.8 M_{\odot}$ for the LS $_{180}$ EOS and low-compactness progenitors and with $\simeq 0.2 M_{\odot}$ more mass for the LS $_{220}$ EOS. The difference decreases the more compact the progenitor star is, with both EOSs predicting almost the same BH formation time and initial BH mass for the most compact progenitor tested here, u75WH02. Nevertheless, O'Connor & Ott (2011) observe that the simulation using the LS $_{220}$ EOS takes longer to collapse into a BH, 285 ms compared to 226 ms for the LS $_{180}$ EOS. Due to the longer accretion time, the simulation using the LS $_{220}$ EOS also collapses with a slightly larger gravitational mass than the one with the LS $_{180}$ EOS, $2.50 M_{\odot}$ to $2.45 M_{\odot}$ of LS $_{180}$. We can understand this by referring back to Figure 5 and noticing that not all of the PNS interior has entropy \tilde{s} , see Equation (6), as in our approach. Some of the PNS innermost regions have entropies lower than \tilde{s} , which also contribute to preventing BH formation. Since for entropies lower than \tilde{s} , the LS $_{180}$ EOS provides lower thermal pressure than the LS $_{220}$ EOS, we expect this to play a second order role into the core-collapse evolution. In fact, we arrive at a similar conclusion performing simulations of core-collapse of the s40WH07 pre-SN progenitor using other EOSs from Hempel et al. (2012), namely the ones that

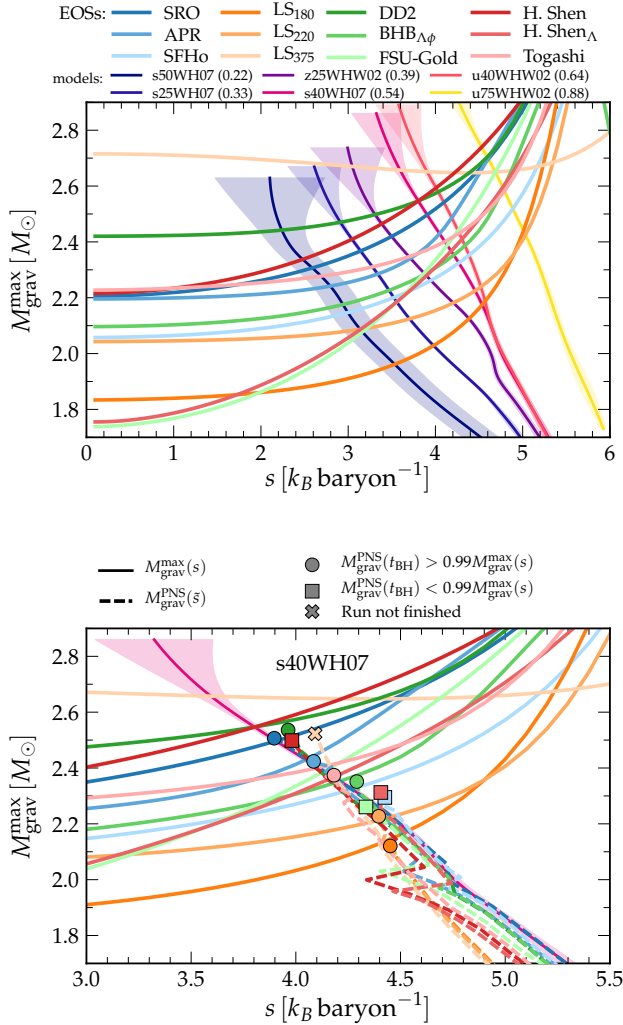


Figure 13. Top: comparison of the maximum gravitational mass supported by a hot NS with constant entropy, $M_{\text{grav}}^{\text{PNS}}$, for selected EOSs in the literature and the average trajectory of the PNS evolution in $M_{\text{grav}}^{\text{PNS}} - \tilde{s}$ space during the core collapse of selected pre-SN progenitor models. Core collapse trajectory in $M_{\text{grav}}^{\text{PNS}} - \tilde{s}$ space depends almost exclusively on the progenitor and, therefore, for a given combination of progenitor and EOS, BH forms near the point where trajectory crosses $M_{\text{grav}}^{\text{max}}(s)$. Bottom: Focus on the s40WH07 pre-SN progenitor evolution after core bounce and simulations performed for the selected EOSs. We mark the BH formation point according to whether BH formed with gravitational mass $M_{\text{grav}}^{\text{PNS}}(t_{\text{BH}})$ above or below the one predicted by $M_{\text{grav}}^{\text{max}}(s)$ multiplied by a factor of 0.99. Only EOSs that have steep increase in $M_{\text{grav}}^{\text{max}}$ with increasing entropy s form BHs with initial mass lower than $0.99 M_{\text{grav}}^{\text{max}}(s)$, but still within 5% of the mass predicted by the average trajectory $M_{\text{grav}}^{\text{PNS}} - \tilde{s}$. BH formation times for the LS180, SFHo, SRO, and DD2 EOSs are, respectively, $t_{\text{BH}} = 0.40, 0.58, 0.81,$ and 1.03 s. The simulation employing the LS₃₇₅ EOS could not be evolved until BH formation due to its proton fraction being limited to $y > 0.035$.

use the TM1, TMA, and FSU-Gold parametrizations of the nuclear interactions, the IU-FSU EOS from [Fattoyev et al. \(2010\)](#), and the H. Shen EOS ([Shen et al. 1998a,b](#)). Those EOSs predict fast increase of $M_{\text{grav}}^{\text{max}}$ with increasing entropy even for $s \lesssim 3 k_B \text{ baryon}^{-1}$, see curves for H. Shen and FSU-Gold in Figure 13. Thus, it is clear our model may need some correction in the initial BH mass for some EOSs of order $\lesssim 0.05 M_{\odot}$ due to the low entropy at the core of the PNS.

A similar pattern to that observed between the LS₁₈₀ and LS₂₂₀ EOSs pair is observed between the H. Shen and LS₃₇₅ EOSs: for pre-SN progenitors with $\xi_{2.5} \lesssim 0.5$ the H. Shen EOS predicts PNSs will collapse into BHs with initial masses $\simeq 0.3 M_{\odot}$ lower than the LS₃₇₅ EOS does. However, for the most compact progenitor stars the BH formation times and initial masses are predicted to be similar for both EOSs, with simulations using the LS₃₇₅ EOS forming BHs with lower initial masses than those that employ the H. Shen EOS. This is another feature that we could have predicted from Figure 13 due to the crossing of $M_{\text{grav}}^{\text{max}}(s)$ for the LS₃₇₅ and H. Shen EOSs near $s = 4.5 k_B \text{ baryon}^{-1}$. Finally, besides our EOS with $m^* = 0.95 m_n$ and $\Delta m^* = 0.30 m_n$, LS₃₇₅ is the only other EOS we have found where $M_{\text{grav}}^{\text{max}}(s)$ does not monotonically increase with entropy s .

Some works studied the effects of mesons and hyperons in BH formation. [Sumiyoshi et al. \(2009\)](#); [Nakazato et al. \(2012\)](#) studied BH formation for the EOSs of [Ishizuka et al. \(2008\)](#), an extension of the [Shen et al. \(1998a,b\)](#) EOS that includes pions and $\Lambda, \Sigma,$ and Ξ hyperons. They showed that the appearance of pions and/or hyperons soften the hot EOS, which decreases the maximum mass supported by a PNS against gravitational collapse, and gives rise to a fast increase in neutrino energies and luminosities at late times when compared to purely hadronic EOSs. [Peres et al. \(2013\)](#) obtained similar results by adding pions and Λ hyperons to the LS₂₂₀ EOS. However, the neutrino luminosity of [Peres et al. \(2013\)](#) for their simulated core collapse using the LS₂₂₀+ Λ EOS was approximately 4 times larger than for the purely hadronic LS₂₂₀ EOS and peaked at $5 \times 10^{54} \text{ erg g}^{-1}$. No other studies we found show similar results.

[Banik et al. \(2014\)](#) compared BH formation time and initial masses for progenitors from [Woosley & Heger \(2007\)](#) for the nuclear H. Shen EOS ([Shen et al. 1998a](#)) and its version containing Λ hyperons ([Shen et al. 1998b](#)). Using the GRID code and a leakage scheme for neutrinos they found that, in general and as expected, Λ hyperons lead to lower BH formation times and initial masses. A follow up study, [Char et al. \(2015\)](#), also simulated spherically symmetric core-collapse for progenitors from [Woosley & Heger \(2007\)](#) using two EOSs containing Λ hyperons, BHB_{Λφ} and H. Shen_Λ. They concluded that BH formation took longer for simulations that used the BHB_{Λφ} EOS than the ones using the H. Shen_Λ EOS because the repulsive $\Lambda - \Lambda$ interactions included in the former and not in the latter made the BHB_{Λφ} EOS stiffer. Nevertheless, an exception was found by [Char et al. \(2015\)](#) for the core collapse of the s40WH07 progeni-

tor, which collapsed into a BH slightly faster when simulated H. Shen $_{\Lambda}$ EOS. In Figure 13 we note that the BHB $_{\Lambda\phi}$ EOS is stiffer than the H. Shen $_{\Lambda}$ EOS for most NSs with a fixed entropy except for a small region with $s \simeq 4.5 k_B$ baryon $^{-1}$, where the H. Shen $_{\Lambda}$ EOS is stiffer. Not surprisingly, this is the region in $M_{\text{grav}}^{\text{PNS}} - \tilde{s}$ parameter space we predict the s40WH07 progenitor will cross during its collapse. Since all other progenitors considered by Char et al. (2015) are less compact than s40WH07 they will all collapse faster in runs that use the H. Shen $_{\Lambda}$ EOS. In fact, Char et al. (2015) observe that the less compact a progenitor is, the larger the difference in both BH formation time and its initial mass, as we expect.

Pan et al. (2018) simulated core collapse of the s40WH07 progenitor until BH formation in both 1D spherically symmetric and 2D axisymmetric geometries. Their runs were also performed using the FLASH software and employed the LS $_{220}$, BHB $_{\Lambda\phi}$, SFHo, and DD2 EOSs. Although their results agree qualitative with ours, the order of collapse for their spherically symmetric runs matches what we would predict with our model, we find that the BH formation time in their runs, see their Table 1, is 13% faster using the LS $_{220}$ EOS and 11% slower using the DD2 EOS. Also, their BHs form with baryonic masses from $0.10 M_{\odot}$ to $0.15 M_{\odot}$ lower than ours and PNS entropies $\tilde{s} \simeq 0.5 k_B$ baryon $^{-1}$ higher than we would expect, see their Figure 5. We attribute these differences to disparate neutrino treatments and resolution used in the two sets of simulations. More importantly, Pan et al. (2018) showed that 2D simulations form BHs at later times and with higher masses than in 1D cases. The mass increase results from convection arising from the negative entropy and lepton fraction gradients which redistribute matter inside the PNS. Note that the Pan et al. (2018) simulation that used the DD2 EOS did not lead to BH formation and exploded 1.3 s after core bounce, which was only possible due to this EOS being able to support a PNS with a large mass. Nevertheless, the qualitative understanding of BH formation gained from the $M_{\text{grav}}^{\text{PNS}}(s)$ relationship is still retained for 2D runs, even if the BH initial masses are shifted to higher values due to convective motion within the PNS. In non-rotating full 3D simulations, it is likely that BHs form with a mass between those predicted from spherically symmetric runs, where no convection is present, and those of axisymmetric runs, where convection may be overestimated due to coherent motion of matter. In fact, Walk et al. (2019) simulated BH formation using full 3D geometry from the collapse of the $40 M_{\odot}$ pre-SN progenitor of Woosley & Heger (2007) using the LS $_{220}$ EOS. In their run, BH formation occurs 570 ms after core bounce, a result that is between the 460 ms of Pan et al. (2018) in spherical symmetry, and 530 ms in ours using the same progenitor and EOS (also in spherical symmetry), and the 704 ms predicted by the axisymmetric simulation of Pan et al. (2018).

We test further our hypothesis that a PNS collapses into a BH once its mass overcomes, or comes close to in some cases, the limit $M_{\text{grav}}^{\text{max}}(\tilde{s})$. We select a single progenitor, s40WH07, and simulate its core collapse using some of the

EOSs found in the literature and discussed in the beginning of this Section. We choose this progenitor as it is expected to form a BH in nature as well as have been repeatedly studied by many groups using unique approximations (O’Connor & Ott 2011; Hempel et al. 2012; Steiner et al. 2013; Banik et al. 2014; Char et al. 2015; Ott et al. 2018; Pan et al. 2018; Walk et al. 2019). Results of the trajectory for each run are shown in the bottom of Figure 13. The simulations performed were evolved until BH formation except for the run using the LS $_{375}$ EOS, which has limitations in its phase space due to the proton fraction being limited to $y > 0.035$. The trajectory in $M_{\text{grav}}^{\text{PNS}} - \tilde{s}$ space for all simulations compare relatively well with our estimates from the SRO EOSs in set s_M . Some differences arise, particularly for the LS EOSs, likely due to different treatments of matter at low densities, which affect the heat transfer of accreted material onto the PNS.

Lastly, we reiterate that in most cases PNSs collapse into a BH within 1% of the gravitational mass value predicted by the crossing of the $M_{\text{grav}}^{\text{PNS}}(\tilde{s})$ and $M_{\text{grav}}^{\text{max}}(s)$ curves. Exceptions for this exist for EOSs which show a fast increase in $M_{\text{grav}}^{\text{max}}(s)$ due to lower thermal pressure contributions from the low entropy innermost region of the PNS. For the s40WH07 progenitor and EOSs used in this Section, see Figure 12, every BH formed with entropy $\tilde{s} \simeq 4 k_B$ baryon $^{-1}$ and with a mass in the range $0.99 - 1.01 M_{\text{grav}}^{\text{max}}(s)$. Exceptions exist for the H. Shen, H. Shen $_{\Lambda}$, SFHo, and FSU-Gold EOSs, which collapsed earlier, but still within 2 – 5% of $M_{\text{grav}}^{\text{max}}(s)$. This explains the results of Hempel et al. (2012); Steiner et al. (2013) that correlate the time for the PNS to collapse into a BH and its mass at formation time with the maximum mass supported by a hot NS with constant $s = 4 k_B$ baryon $^{-1}$ entropy.

5. CONCLUSIONS

To date many works have shed light on the intricate relationships between the EOS of dense matter and the core collapse evolution of a massive star and resulting GW and neutrino signals (Sekiguchi & Shibata 2005; Sumiyoshi et al. 2006; Ott et al. 2011; O’Connor & Ott 2011; Hempel et al. 2012; Steiner et al. 2013; Cerdá-Durán et al. 2013; Pan et al. 2018; Warren et al. 2019). We build upon on these studies by performing systematic spherically symmetric CCSN simulations of 51 non-rotating pre-SN progenitors with 60 EOSs until BH formation.

For the 45 progenitors of Sukhbold et al. (2018) used in this study, we simulate the collapse employing the baseline Skyrme-type SRO EOS of Schneider et al. (2019a) using the Newtonian FLASH code with a modified GR potential from Marek et al. (2006) and an energy-dependent, two-moment neutrino transport. We observe that in almost every case, the recently formed PNS becomes gravitationally unstable and collapses into a BH soon after the gravitational mass of the PNS exceeds $M_{\text{grav}}^{\text{max}}(\tilde{s})$. Here $M_{\text{grav}}^{\text{max}}(\tilde{s})$ is the maximum mass supported by a hot PNS with constant entropy \tilde{s} , where \tilde{s} is the most common entropy value within the PNS. Interestingly, the trajectory traced by the PNS in $M_{\text{grav}}^{\text{PNS}} - \tilde{s}$ space by each progenitor is close to a straight line where the

entropy decreases as the PNS mass increases. These lines are approximately ordered by progenitor compactness and their slopes are slightly steeper for progenitors that maintain large accretion rates throughout collapse. Thus, studying the collapse of a compact pre-SN progenitor star using a single EOS may be enough to infer when BH formation will take place for most other EOSs.

For several of the compact progenitors, we test and confirm the suitability of employing the general relativistic effective potential in order to model BH formation by comparing the core-collapse evolution to fully general relativistic simulations using GR1D. We observe that employing the “Case A” of Marek et al. (2006) the effective potential slightly underestimates the BH formation time by $\sim 4\%$ for the most compact progenitors are upwards of $\sim 16\%$ for the least compact ones. We tested modifications to the effective potential, and while we were able to achieve better matching to the central density evolution using “Case A_ϕ ”, a modification of the standard “Case A” of Marek et al. (2006), most quantities of interest, like the neutrino luminosities, are still best reproduced with the standard “Case A”. Moreover, we reaffirm that although compactness, ξ_M , is a good indicator of BH formation time and initial BH mass (O’Connor & Ott 2011), the temporal evolution of the spectra of neutrinos emitted, the accretion rate, and shock radius are not described well by this single parameter. As others have pointed out, at least two parameters may be necessary to characterize the core collapse outcome of a progenitor (Ertl et al. 2016; Ebinger et al. 2018).

To better understand EOS effects in a PNS evolution until BH formation we simulate the core collapse of six compact progenitors of Woosley et al. (2002); Woosley & Heger (2007). For each progenitor 49 simulations were performed, one simulation using the baseline SRO EOS, 24 simulations where the zero-temperature component of the EOS was altered, set s_P , and another 24 simulations where the thermal component of the EOS was altered, set s_M . For the least compact progenitor star in our set, s50WHW07 with compactness $\xi_M = 0.22$, both EOS sets s_M and s_P predicted BH would form between $3.4\text{ s} \lesssim t_{\text{BH}} \lesssim 5.2\text{ s}$ after core bounce. However, for the most compact progenitor in the set, u75WH02 with compactness $\xi_M = 0.88$, BH formation times were in the $0.40\text{ s} \lesssim t_{\text{BH}} \lesssim 0.46\text{ s}$ range for EOSs in set s_P and in the $0.24\text{ s} \lesssim t_{\text{BH}} \lesssim 0.59\text{ s}$ range for EOSs in set s_M . Again, in almost all of these simulations, BH formation occurred only after the PNS gravitational mass surpassed $M_{\text{grav}}^{\text{max}}(\tilde{s})$ or was within 1% of this value and the trajectory in $M_{\text{grav}}^{\text{PNS}} - \tilde{s}$ space was very similar for each progenitor regardless of EOS.

Combining the results above allowed us to find a simple explanation for why BH formation times differ so much for the two EOS sets s_M and s_P for the core collapse of more compact progenitors while being rather similar for less compact ones. For EOSs in set s_M , which differ only in their thermal component, the differences between $M_{\text{grav}}^{\text{max}}(s)$ at entropies $s \gtrsim 3 k_B \text{ baryon}^{-1}$ ($s \lesssim 3 k_B \text{ baryon}^{-1}$) are large

(small). Meanwhile, the opposite behavior is observed for EOSs in set s_P . Because, to a good approximation, BHs from CCSNe form soon after the PNS path in $M_{\text{grav}}^{\text{PNS}} - \tilde{s}$ space crosses $M_{\text{grav}}^{\text{max}}(s)$ for the EOS used in the simulation, initial BH masses will be more similar amongst EOSs that predict similar masses at the crossing location. This single observation allows us to also explain the patterns seen in CCSN simulations of many previous studies (Sumiyoshi et al. 2006; Nakazato et al. 2012; Char et al. 2015; Pan et al. 2018), including that of O’Connor & Ott (2011), who simulated core-collapse of over 100 progenitors using 4 different EOSs, as well as to explain why BH formation times and initial gravitational masses for the s40WH07 progenitor correlate with $M_{\text{grav}}^{\text{max}}(s = 4 k_B \text{ baryon}^{-1})$, the maximum gravitational mass possible for a hot NS with constant $s = 4 k_B \text{ baryon}^{-1}$ entropy (Hempel et al. 2012; Steiner et al. 2013).

Recently, Yasin et al. (2018); Schneider et al. (2019a) showed that EOSs that are softer with increasing temperatures increase the probability of a successful CCSN explosion since these EOSs lead to more compact PNSs which, in turn, increase neutrino luminosities and heating behind the shock. Here we show that these same EOSs also lead to BH formation with lower initial masses than EOSs that become stiffer at the large temperatures found within PNSs. In this work we focused most on Skyrme-type models, where the temperature dependence of the EOS is almost exclusively dictated by the effective mass of nucleons which are simply a function of nucleon density. However, more realistic EOSs will have a more intricate interplay between temperature, effective mass, and thermal pressure. In fact, ab-initio calculations by Carbone (2019); Carbone & Schwenk (2019) show that at higher densities and temperatures, nucleon effective masses may become larger than their vacuum values.

The combined results of Carbone (2019); Carbone & Schwenk (2019) and Yasin et al. (2018); Schneider et al. (2019a) imply that successful supernovae explosions followed by BH formation may be a common evolutionary end path of the core collapse of massive stars. Moreover, at the high temperatures and densities found within PNSs, muons (Bollig et al. 2017), pions and hyperons (Sumiyoshi et al. 2009; Nakazato et al. 2012; Peres et al. 2013; Banik et al. 2014; Char et al. 2015), and phase transitions to quark matter (Sagert et al. 2009; Hempel et al. 2016; Fischer et al. 2018; Aloy et al. 2019) may play a significant role. The appearance of massive particles could facilitate supernovae explosions by speeding up PNS contraction and, thus, increasing neutrino emission (Sumiyoshi et al. 2009; Nakazato et al. 2012; Peres et al. 2013). Also, massive leptons and hadrons, in addition to the thermal neutrinos present in the PNS, soften the EOS at high densities and temperatures, which decrease the maximum hot PNS mass. Thus, one may expect that for such an EOS, the maximum supported hot PNS mass $M_{\text{grav}}^{\text{max}}(s)$ at a large entropy could be lower than the cold NS maximum mass, as seen here for the LS₃₇₅ EOS and the EOS in set s_M with $m^* = 0.95 m_n$ and $\Delta m^* = 0.30 m_n$. This is also true for the LS₂₂₀+ Λ EOS as shown by Oertel

et al. (2016), who studied amongst other subjects the effects of adding pions and/or hyperons on the maximum mass of cold ($T = 0$) and hot PNSs ($s = 4 k_B$ baryon $^{-1}$). However, for all other EOSs studied here and by Oertel et al. (2016) $M_{\text{grav}}^{\text{max}}(s = 4 k_B \text{ baryon}^{-1}) > M_{\text{grav}}^{\text{max}}(T = 0)$.

We speculate on the possible core-collapse outcomes considering that the true EOS of dense matter has a large enough decrease in maximum mass supported by a hot NS. In such a case, there could be a combination of EOS and compact pre-SN progenitor which either triggers a neutrino-driven or magneto-rotational explosion that is both strong and early (resulting in no fallback), while producing a PNS that would collapse into BH with mass *lower* than the maximum mass supported by a cold NS. Peres et al. (2013) find a situation similar to this one in their core-collapse of a $40 M_{\odot}$ progenitor star with the LS₂₂₀+ Λ EOS, although in their simulation the BH would continue to accrete matter. Nevertheless, this progenitor forms a BH with initial mass $M_{\text{grav}}^{\text{BH}} \simeq 1.80 M_{\odot}$. The initial BH mass is estimated from the baryonic mass and neutrino luminosities presented in Peres et al. (2013) assuming that (1) all of the gravitational binding energy is radiated by neutrinos and (2) that the neutrino luminosity remains flat beyond 150 ms until BH formation time. This value is lower than the maximum supported cold NS mass $M_{\text{grav}}^{\text{PNS}} \simeq 1.91 M_{\odot}$ and in line with the value expected for this EOS for a hot $s = 4 k_B$ baryon $^{-1}$ NS (Oertel et al. 2016).

Despite the curious picture described above, most currently available realistic EOSs predict a scenario where the maximum mass supported by a hot PNS increases with temperature and, thus, it is likely that the higher the compactness of the pre-SN progenitor is, the more massive the PNS will be when it forms a BH. The PNS mass evolution as well as the BH formation time and its initial mass may be deduced for a failed galactic supernova if their neutrino signal is detected (Kachelrieß et al. 2005; Sumiyoshi et al. 2007; Suwa et al. 2019). As we have shown here (see Figures 10, 12, and 13), the PNS path in $M_{\text{grav}}^{\text{PNS}} - \tilde{s}$ phase space is mostly a function of the compactness of the pre-SN progenitor star while the BH formation time is a function of the EOS. Therefore, an observation of the compactness, for example, via neutrinos (Horiuchi et al. 2017), from a failed galactic supernova could then be used to impose strong constraints both on the structure of the innermost regions of the progenitor star as well as the temperature dependence of the EOS, even more so if coupled to GW detections. The final BH mass, on the other hand, may not be achieved for years after the core col-

lapse and will be function of more than just the compactness of the progenitor since the total ejected and accreted masses depend on the total energy transferred by neutrinos to the shock and the structure of the progenitor star.

We emphasize that all of our simulations were performed considering non-rotating spherically symmetric stars and that CCSNe are fundamentally multidimensional systems. Effects due to rotation and convection, both of which are expected to increase the maximum PNS mass before its collapse into a BH (Cook et al. 1994; Morrison et al. 2004; Sekiguchi & Shibata 2005; O’Connor & Ott 2011; Pan et al. 2018; Obergaulinger & Aloy 2019; Walk et al. 2019; Nagakura et al. 2019), should be addressed in the future. In extreme cases rotation may lead to a significant increase in the supported gravitational mass for cold NSs (Espino & Paschalidis 2019; Szekudlarek et al. 2019). Even though extreme rotation rates may be rare in stellar collapse, a picture favored by binary BH merger detections (Abbott et al. 2019a) and stellar evolution scenarios (Belczynski et al. 2019; Fuller & Ma 2019), its effects are not uniform across EOSs (O’Connor & Ott 2011; Richers et al. 2017). Thus, an extra axis to the $M_{\text{grav}}^{\text{PNS}} - \tilde{s}$ diagram has to be added to address its impact on PNS evolution. Finally, although the consequences of convection within the PNS may not be as extreme as that of rotation, it still could be the decisive factor between a successful or a failed CCSN in some cases (Pan et al. 2018; Nagakura et al. 2019) and shift the $M_{\text{grav}}^{\text{max}}(s)$ relations computed for each EOS and/or progenitor.

ACKNOWLEDGMENTS

This work benefited from interesting and helpful discussions with M. Prakash, C. Constantinou, MK.L. Warren, and H. Yasin. The authors acknowledge support from the Swedish Research Council (Project No. 2018-04575). The simulations were performed on resources provided by the Swedish National Infrastructure for Computing (SNIC) at PDC and NSC. The software used in this work was in part developed by the DOE NNSA-ASC OASCR Flash Center at the University of Chicago. SMC is supported by the U.S. Department of Energy, Office of Science, Office of Nuclear Physics, under Award Numbers DE-SC0015904 and DE-SC0017955.

Software: FLASH (Fryxell et al. 2000; Dubey et al. 2009; Couch 2013; O’Connor et al. 2018), GR1D (O’Connor & Ott 2010; O’Connor 2015), Matplotlib (Hunter 2007), NuLib (O’Connor 2015), SROEOS (Schneider et al. 2017), scikit-learn (Pedregosa et al. 2011).

REFERENCES

- Abbott, B. P., Abbott, R., Abbott, T. D., et al. 2019a, PhRvX, 9, 031040, doi: [10.1103/PhysRevX.9.031040](https://doi.org/10.1103/PhysRevX.9.031040)
- . 2019b, PhRvX, 9, 011001, doi: [10.1103/PhysRevX.9.011001](https://doi.org/10.1103/PhysRevX.9.011001)
- Akmal, A., Pandharipande, V. R., & Ravenhall, D. G. 1998, PhRvC, 58, 1804, doi: [10.1103/PhysRevC.58.1804](https://doi.org/10.1103/PhysRevC.58.1804)
- Aloy, M. A., Ibáñez, J. M., Sanchis-Gual, N., et al. 2019, MNRAS, 484, 4980, doi: [10.1093/mnras/stz293](https://doi.org/10.1093/mnras/stz293)

- Antoniadis, J., Freire, P. C. C., Wex, N., et al. 2013, *Sci*, 340, 1233232, doi: [10.1126/science.1233232](https://doi.org/10.1126/science.1233232)
- Banik, S. 2014, *PhRvC*, 89, 035807, doi: [10.1103/PhysRevC.89.035807](https://doi.org/10.1103/PhysRevC.89.035807)
- Banik, S., Hempel, M., & Bandyopadhyay, D. 2014, *ApJS*, 214, 22, doi: [10.1088/0067-0049/214/2/22](https://doi.org/10.1088/0067-0049/214/2/22)
- Belczynski, K., Holz, D. E., Bulik, T., & O’Shaughnessy, R. 2016, *Natur*, 534, 512, doi: [10.1038/nature18322](https://doi.org/10.1038/nature18322)
- Belczynski, K., Wiktorowicz, G., Fryer, C. L., Holz, D. E., & Kalogera, V. 2012, *ApJ*, 757, 91, doi: [10.1088/0004-637X/757/1/91](https://doi.org/10.1088/0004-637X/757/1/91)
- Belczynski, K., Klencki, J., Fields, C. E., et al. 2019, arXiv:1706.07053 [astro-ph, physics:gr-qc]. <https://arxiv.org/abs/1706.07053>
- Bethe, H. A. 1990, *RvMP*, 62, 801, doi: [10.1103/RevModPhys.62.801](https://doi.org/10.1103/RevModPhys.62.801)
- Bethe, H. A., & Wilson, J. R. 1985, *ApJ*, 295, 14, doi: [10.1086/163343](https://doi.org/10.1086/163343)
- Bollig, R., Janka, H.-T., Lohs, A., et al. 2017, *PhRvL*, 119, 242702, doi: [10.1103/PhysRevLett.119.242702](https://doi.org/10.1103/PhysRevLett.119.242702)
- Bruenn, S. W. 1985, *ApJS*, 58, 771, doi: [10.1086/191056](https://doi.org/10.1086/191056)
- Buras, R., Janka, H.-T., Rampp, M., & Kifonidis, K. 2006, *A&A*, 457, 281, doi: [10.1051/0004-6361:20054654](https://doi.org/10.1051/0004-6361:20054654)
- Burrows, A. 1986, *ApJ*, 300, 488, doi: [10.1086/163826](https://doi.org/10.1086/163826)
- . 1988, *ApJ*, 334, 891, doi: [10.1086/166885](https://doi.org/10.1086/166885)
- Burrows, A., Radice, D., Vartanyan, D., et al. 2020, *MNRAS*, 491, 2715, doi: [10.1093/mnras/stz3223](https://doi.org/10.1093/mnras/stz3223)
- Burrows, A., Reddy, S., & Thompson, T. A. 2006, *NuPhA*, 777, 356, doi: [10.1016/j.nuclphysa.2004.06.012](https://doi.org/10.1016/j.nuclphysa.2004.06.012)
- Burrows, A., Vartanyan, D., Dolence, J. C., Skinner, M. A., & Radice, D. 2018, *SSRv*, 214, 33, doi: [10.1007/s11214-017-0450-9](https://doi.org/10.1007/s11214-017-0450-9)
- Carbone, A. 2019, arXiv:1908.04736 [astro-ph, physics:gr-qc, physics:nucl-ex, physics:nucl-th]. <https://arxiv.org/abs/1908.04736>
- Carbone, A., & Schwenk, A. 2019, *PhRvC*, 100, 025805, doi: [10.1103/PhysRevC.100.025805](https://doi.org/10.1103/PhysRevC.100.025805)
- Cardall, C. Y., Endeve, E., & Mezzacappa, A. 2013, *PhRvD*, 88, 023011, doi: [10.1103/PhysRevD.88.023011](https://doi.org/10.1103/PhysRevD.88.023011)
- Cerdá-Durán, P., DeBrye, N., Aloy, M. A., Font, J. A., & Obergaulinger, M. 2013, *ApJ*, 779, L18, doi: [10.1088/2041-8205/779/2/L18](https://doi.org/10.1088/2041-8205/779/2/L18)
- Char, P., Banik, S., & Bandyopadhyay, D. 2015, *ApJ*, 809, 116, doi: [10.1088/0004-637X/809/2/116](https://doi.org/10.1088/0004-637X/809/2/116)
- Colgate, S. A., & White, R. H. 1966, *ApJ*, 143, 626, doi: [10.1086/148549](https://doi.org/10.1086/148549)
- Constantinou, C., Muccioli, B., Prakash, M., & Lattimer, J. M. 2014, *PhRvC*, 89, 065802, doi: [10.1103/PhysRevC.89.065802](https://doi.org/10.1103/PhysRevC.89.065802)
- Cook, G. B., Shapiro, S. L., & Teukolsky, S. A. 1994, *ApJ*, 424, 823, doi: [10.1086/173934](https://doi.org/10.1086/173934)
- Couch, S. 2019, in prep.
- Couch, S. M. 2013, *ApJ*, 765, 29, doi: [10.1088/0004-637X/765/1/29](https://doi.org/10.1088/0004-637X/765/1/29)
- Couch, S. M., Warren, M. L., & O’Connor, E. P. 2019, arXiv:1902.01340 [astro-ph]. <https://arxiv.org/abs/1902.01340>
- Danielewicz, P. 2002, *Sci*, 298, 1592, doi: [10.1126/science.1078070](https://doi.org/10.1126/science.1078070)
- Dessart, L., Burrows, A., Livne, E., & Ott, C. D. 2006, *ApJ*, 645, 534, doi: [10.1086/504068](https://doi.org/10.1086/504068)
- Dimmelmeier, H., Font, J. A., & Müller, E. 2002a, *A&A*, 388, 917, doi: [10.1051/0004-6361:20020563](https://doi.org/10.1051/0004-6361:20020563)
- . 2002b, *A&A*, 393, 523, doi: [10.1051/0004-6361:20021053](https://doi.org/10.1051/0004-6361:20021053)
- Dimmelmeier, H., Novak, J., Font, J. A., Ibáñez, J. M., & Müller, E. 2005, *PhRvD*, 71, 064023, doi: [10.1103/PhysRevD.71.064023](https://doi.org/10.1103/PhysRevD.71.064023)
- Dubey, A., Antypas, K., Ganapathy, M. K., et al. 2009, *ParC*, 35, 512, doi: [10.1016/j.parco.2009.08.001](https://doi.org/10.1016/j.parco.2009.08.001)
- Ebinger, K., Curtis, S., Fröhlich, C., et al. 2018, *ApJ*, 870, 1, doi: [10.3847/1538-4357/aae7c9](https://doi.org/10.3847/1538-4357/aae7c9)
- Ertl, T., Janka, H.-T., Woosley, S. E., Sukhbold, T., & Ugliano, M. 2016, *ApJ*, 818, 124, doi: [10.3847/0004-637X/818/2/124](https://doi.org/10.3847/0004-637X/818/2/124)
- Esin, A. A., Narayan, R., Cui, W., Grove, J. E., & Zhang, S.-N. 1998, *ApJ*, 505, 854, doi: [10.1086/306186](https://doi.org/10.1086/306186)
- Espino, P. L., & Paschalidis, V. 2019, *PhRvD*, 99, 083017, doi: [10.1103/PhysRevD.99.083017](https://doi.org/10.1103/PhysRevD.99.083017)
- Fattoyev, F. J., Horowitz, C. J., Piekarewicz, J., & Shen, G. 2010, *PhRvC*, 82, 055803, doi: [10.1103/PhysRevC.82.055803](https://doi.org/10.1103/PhysRevC.82.055803)
- Fischer, T., Martínez-Pinedo, G., Hempel, M., & Liebendörfer, M. 2012, *PhRvD*, 85, 083003, doi: [10.1103/PhysRevD.85.083003](https://doi.org/10.1103/PhysRevD.85.083003)
- Fischer, T., Whitehouse, S. C., Mezzacappa, A., Thielemann, F.-K., & Liebendörfer, M. 2009, *A&A*, 499, 1, doi: [10.1051/0004-6361/200811055](https://doi.org/10.1051/0004-6361/200811055)
- . 2010, *A&A*, 517, A80, doi: [10.1051/0004-6361/200913106](https://doi.org/10.1051/0004-6361/200913106)
- Fischer, T., Bastian, N.-U. F., Wu, M.-R., et al. 2018, *NatAs*, 2, 980, doi: [10.1038/s41550-018-0583-0](https://doi.org/10.1038/s41550-018-0583-0)
- Fryxell, B., Olson, K., Ricker, P., et al. 2000, *ApJS*, 131, 273, doi: [10.1086/317361](https://doi.org/10.1086/317361)
- Fuller, J., & Ma, L. 2019, *ApJ*, 881, L1, doi: [10.3847/2041-8213/ab339b](https://doi.org/10.3847/2041-8213/ab339b)
- Gossan, S. E., Fuller, J., & Roberts, L. F. 2019, *MNRAS*, stz3243, doi: [10.1093/mnras/stz3243](https://doi.org/10.1093/mnras/stz3243)
- Granqvist, E. 2019, Stockholm University Bachelor thesis: Approximating General Relativistic Effects in Newtonian Hydrodynamic Supernova Simulations, <http://urn.kb.se/resolve?urn=urn:nbn:se:su:diva-169517>
- Hempel, M., Fischer, T., Schaffner-Bielich, J., & Liebendörfer, M. 2012, *ApJ*, 748, 70, doi: [10.1088/0004-637X/748/1/70](https://doi.org/10.1088/0004-637X/748/1/70)
- Hempel, M., Heinemann, O., Yudin, A., et al. 2016, *PhRvD*, 94, 103001, doi: [10.1103/PhysRevD.94.103001](https://doi.org/10.1103/PhysRevD.94.103001)
- Horiuchi, S., Nakamura, K., Takiwaki, T., & Kotake, K. 2017, *JPhG*, 44, 114001, doi: [10.1088/1361-6471/aa8f1f](https://doi.org/10.1088/1361-6471/aa8f1f)
- Horowitz, C. J. 2002, *PhRvD*, 65, 043001, doi: [10.1103/PhysRevD.65.043001](https://doi.org/10.1103/PhysRevD.65.043001)
- Hüdepohl, L. 2014, Dissertation, Technische Universität München, München
- Hunter, J. D. 2007, *CSE*, 9, 90, doi: [10.1109/MCSE.2007.55](https://doi.org/10.1109/MCSE.2007.55)

- Ishizuka, C., Ohnishi, A., Tsubakihara, K., Sumiyoshi, K., & Yamada, S. 2008, *JPhG*, 35, 085201, doi: [10.1088/0954-3899/35/8/085201](https://doi.org/10.1088/0954-3899/35/8/085201)
- Janka, H.-T. 2001, *A&A*, 368, 527, doi: [10.1051/0004-6361:20010012](https://doi.org/10.1051/0004-6361:20010012)
- . 2012, *ARNPS*, 62, 407, doi: [10.1146/annurev-nucl-102711-094901](https://doi.org/10.1146/annurev-nucl-102711-094901)
- Jones, E., Oliphant, T., Peterson, P., et al. 2001, *SciPy: Open Source Scientific Tools for Python*. <http://www.scipy.org/>
- Kachelrieß, M., Tomàs, R., Buras, R., et al. 2005, *PhRvD*, 71, 063003, doi: [10.1103/PhysRevD.71.063003](https://doi.org/10.1103/PhysRevD.71.063003)
- Kitaura, F. S., Janka, H.-T., & Hillebrandt, W. 2006, *A&A*, 450, 345, doi: [10.1051/0004-6361:20054703](https://doi.org/10.1051/0004-6361:20054703)
- Kubota, A., Tanaka, Y., Makishima, K., et al. 1998, *PASJ*, 50, 667, doi: [10.1093/pasj/50.6.667](https://doi.org/10.1093/pasj/50.6.667)
- Lattimer, J. M. 1981, *ARNPS*, 31, 337, doi: [10.1146/annurev.ns.31.120181.002005](https://doi.org/10.1146/annurev.ns.31.120181.002005)
- Lattimer, J. M., & Prakash, M. 2000, *PhR*, 333-334, 121, doi: [10.1016/S0370-1573\(00\)00019-3](https://doi.org/10.1016/S0370-1573(00)00019-3)
- Lattimer, J. M., & Swesty, F. D. 1991, *NuPhA*, 535, 331, doi: [10.1016/0375-9474\(91\)90452-C](https://doi.org/10.1016/0375-9474(91)90452-C)
- Liebrandt, M., Messer, O. E. B., Mezzacappa, A., et al. 2004, *ApJS*, 150, 263, doi: [10.1086/380191](https://doi.org/10.1086/380191)
- Liebrandt, M., Mezzacappa, A., & Thielemann, F.-K. 2001, *PhRvD*, 63, 104003, doi: [10.1103/PhysRevD.63.104003](https://doi.org/10.1103/PhysRevD.63.104003)
- Liebrandt, M., Rampp, M., Janka, H.-T., & Mezzacappa, A. 2005, *ApJ*, 620, 840, doi: [10.1086/427203](https://doi.org/10.1086/427203)
- Liebrandt, M., Rosswog, S., & Thielemann, F.-K. 2002, *ApJS*, 141, 229, doi: [10.1086/339872](https://doi.org/10.1086/339872)
- Mandel, I., & de Mink, S. E. 2016, *MNRAS*, 458, 2634, doi: [10.1093/mnras/stw379](https://doi.org/10.1093/mnras/stw379)
- Marek, A., Dimmelmeier, H., Janka, H.-T., Müller, E., & Buras, R. 2006, *A&A*, 445, 273, doi: [10.1051/0004-6361:20052840](https://doi.org/10.1051/0004-6361:20052840)
- Margueron, J., Hoffmann Casali, R., & Gulminelli, F. 2018, *PhRvC*, 97, 025805, doi: [10.1103/PhysRevC.97.025805](https://doi.org/10.1103/PhysRevC.97.025805)
- Martínez-Pinedo, G., Fischer, T., Lohs, A., & Huther, L. 2012, *PhRvL*, 109, 251104, doi: [10.1103/PhysRevLett.109.251104](https://doi.org/10.1103/PhysRevLett.109.251104)
- Melson, T., Janka, H.-T., Bollig, R., et al. 2015, *ApJ*, 808, L42, doi: [10.1088/2041-8205/808/2/L42](https://doi.org/10.1088/2041-8205/808/2/L42)
- Miller, M. C., Lamb, F. K., Dittmann, A. J., et al. 2019, *ApJ*, 887, L24, doi: [10.3847/2041-8213/ab50c5](https://doi.org/10.3847/2041-8213/ab50c5)
- Morozova, V., Radice, D., Burrows, A., & Vartanyan, D. 2018, *ApJ*, 861, 10, doi: [10.3847/1538-4357/aac5f1](https://doi.org/10.3847/1538-4357/aac5f1)
- Morrison, I. A., Baumgarte, T. W., & Shapiro, S. L. 2004, *ApJ*, 610, 941, doi: [10.1086/421897](https://doi.org/10.1086/421897)
- Nagakura, H., Burrows, A., Radice, D., & Vartanyan, D. 2019, *arXiv:1912.07615* [astro-ph]. <https://arxiv.org/abs/1912.07615>
- Nakazato, K., Furusawa, S., Sumiyoshi, K., et al. 2012, *ApJ*, 745, 197, doi: [10.1088/0004-637X/745/2/197](https://doi.org/10.1088/0004-637X/745/2/197)
- Nakazato, K., Sumiyoshi, K., Suzuki, H., et al. 2013, *ApJS*, 205, 2, doi: [10.1088/0067-0049/205/1/2](https://doi.org/10.1088/0067-0049/205/1/2)
- Nakazato, K., & Suzuki, H. 2019, *ApJ*, 878, 25, doi: [10.3847/1538-4357/ab1d4b](https://doi.org/10.3847/1538-4357/ab1d4b)
- Nakazato, K., Suzuki, H., & Togashi, H. 2018, *PhRvC*, 97, 035804, doi: [10.1103/PhysRevC.97.035804](https://doi.org/10.1103/PhysRevC.97.035804)
- Nättilä, J., Steiner, A. W., Kajava, J. J. E., Suleimanov, V. F., & Poutanen, J. 2016, *A&A*, 591, A25, doi: [10.1051/0004-6361/201527416](https://doi.org/10.1051/0004-6361/201527416)
- Obergaulinger, M., & Aloy, M. Á. 2019, *arXiv:1909.01105* [astro-ph]. <https://arxiv.org/abs/1909.01105>
- O'Connor, E. 2015, *ApJS*, 219, 24, doi: [10.1088/0067-0049/219/2/24](https://doi.org/10.1088/0067-0049/219/2/24)
- O'Connor, E., & Ott, C. D. 2010, *CQGra*, 27, 114103, doi: [10.1088/0264-9381/27/11/114103](https://doi.org/10.1088/0264-9381/27/11/114103)
- . 2011, *ApJ*, 730, 70, doi: [10.1088/0004-637X/730/2/70](https://doi.org/10.1088/0004-637X/730/2/70)
- . 2013, *ApJ*, 762, 126, doi: [10.1088/0004-637X/762/2/126](https://doi.org/10.1088/0004-637X/762/2/126)
- O'Connor, E., Bollig, R., Burrows, A., et al. 2018, *JPhG*, 45, 104001, doi: [10.1088/1361-6471/aadeae](https://doi.org/10.1088/1361-6471/aadeae)
- O'Connor, E. P., & Couch, S. M. 2018a, *ApJ*, 854, 63, doi: [10.3847/1538-4357/aaa893](https://doi.org/10.3847/1538-4357/aaa893)
- . 2018b, *ApJ*, 865, 81, doi: [10.3847/1538-4357/aadcf7](https://doi.org/10.3847/1538-4357/aadcf7)
- Oertel, M., Gulminelli, F., Providência, C., & Raduta, A. R. 2016, *EPJA*, 52, 50, doi: [10.1140/epja/i2016-16050-1](https://doi.org/10.1140/epja/i2016-16050-1)
- Ott, C. D., Roberts, L. F., da Silva Schneider, A., et al. 2018, *ApJ*, 855, L3, doi: [10.3847/2041-8213/aaa967](https://doi.org/10.3847/2041-8213/aaa967)
- Ott, C. D., Reisswig, C., Schnetter, E., et al. 2011, *PhRvL*, 106, 161103, doi: [10.1103/PhysRevLett.106.161103](https://doi.org/10.1103/PhysRevLett.106.161103)
- Pan, K.-C., Liebrandt, M., Couch, S. M., & Thielemann, F.-K. 2018, *ApJ*, 857, 13, doi: [10.3847/1538-4357/aab71d](https://doi.org/10.3847/1538-4357/aab71d)
- Pedregosa, F., Varoquaux, G., Gramfort, A., et al. 2011, *JMLR*, 12, 2825
- Peres, B., Oertel, M., & Novak, J. 2013, *PhRvD*, 87, 043006, doi: [10.1103/PhysRevD.87.043006](https://doi.org/10.1103/PhysRevD.87.043006)
- Portegies Zwart, S. F., & McMillan, S. L. W. 2000, *ApJ*, 528, L17, doi: [10.1086/312422](https://doi.org/10.1086/312422)
- Prakash, M., Bombaci, I., Prakash, M., et al. 1997, *PhR*, 280, 1, doi: [10.1016/S0370-1573\(96\)00023-3](https://doi.org/10.1016/S0370-1573(96)00023-3)
- Rampp, M., & Janka, H.-T. 2002, *A&A*, 396, 361, doi: [10.1051/0004-6361:20021398](https://doi.org/10.1051/0004-6361:20021398)
- Richers, S., Ott, C. D., Abdikamalov, E., O'Connor, E., & Sullivan, C. 2017, *PhRvD*, 95, 063019, doi: [10.1103/PhysRevD.95.063019](https://doi.org/10.1103/PhysRevD.95.063019)
- Roberts, L. F. 2012, *ApJ*, 755, 126, doi: [10.1088/0004-637X/755/2/126](https://doi.org/10.1088/0004-637X/755/2/126)
- Roberts, L. F., & Reddy, S. 2016, in *Handbook of Supernovae*, ed. A. W. Alsabti & P. Murdin (Cham: Springer International Publishing), 1–31. http://link.springer.com/10.1007/978-3-319-20794-0_5-1
- Roberts, L. F., Shen, G., Cirigliano, V., et al. 2012, *PhRvL*, 108, 061103, doi: [10.1103/PhysRevLett.108.061103](https://doi.org/10.1103/PhysRevLett.108.061103)
- Rodríguez, C. L., Morscher, M., Pattabiraman, B., et al. 2015, *PhRvL*, 115, 051101, doi: [10.1103/PhysRevLett.115.051101](https://doi.org/10.1103/PhysRevLett.115.051101)

- Sagert, I., Fischer, T., Hempel, M., et al. 2009, *PhRvL*, 102, 081101, doi: [10.1103/PhysRevLett.102.081101](https://doi.org/10.1103/PhysRevLett.102.081101)
- Schneider, A. S., Constantinou, C., Muccioli, B., & Prakash, M. 2019a, *PhRvC*, 100, 025803, doi: [10.1103/PhysRevC.100.025803](https://doi.org/10.1103/PhysRevC.100.025803)
- Schneider, A. S., Roberts, L. F., & Ott, C. D. 2017, *PhRvC*, 96, 065802, doi: [10.1103/PhysRevC.96.065802](https://doi.org/10.1103/PhysRevC.96.065802)
- Schneider, A. S., Roberts, L. F., Ott, C. D., & O'Connor, E. 2019b, *PhRvC*, 100, 055802, doi: [10.1103/PhysRevC.100.055802](https://doi.org/10.1103/PhysRevC.100.055802)
- Scholberg, K. 2012, *ARNPS*, 62, 81, doi: [10.1146/annurev-nucl-102711-095006](https://doi.org/10.1146/annurev-nucl-102711-095006)
- Sekiguchi, Y.-i., & Shibata, M. 2005, *PhRvD*, 71, 084013, doi: [10.1103/PhysRevD.71.084013](https://doi.org/10.1103/PhysRevD.71.084013)
- Shen, H., Toki, H., Oyamatsu, K., & Sumiyoshi, K. 1998a, *NuPhA*, 637, 435, doi: [10.1016/S0375-9474\(98\)00236-X](https://doi.org/10.1016/S0375-9474(98)00236-X)
- . 1998b, *PThPh*, 100, 1013, doi: [10.1143/PTP.100.1013](https://doi.org/10.1143/PTP.100.1013)
- . 2011, *ApJS*, 197, 20, doi: [10.1088/0067-0049/197/2/20](https://doi.org/10.1088/0067-0049/197/2/20)
- Shibata, M., Kiuchi, K., Sekiguchi, Y.-i., & Suwa, Y. 2011, *PThPh*, 125, 1255, doi: [10.1143/PTP.125.1255](https://doi.org/10.1143/PTP.125.1255)
- Steiner, A. W., Hempel, M., & Fischer, T. 2013, *ApJ*, 774, 17, doi: [10.1088/0004-637X/774/1/17](https://doi.org/10.1088/0004-637X/774/1/17)
- Stevenson, S., Vigna-Gómez, A., Mandel, I., et al. 2017, *NatCo*, 8, 14906, doi: [10.1038/ncomms14906](https://doi.org/10.1038/ncomms14906)
- Sukhbold, T., Woosley, S. E., & Heger, A. 2018, *ApJ*, 860, 93, doi: [10.3847/1538-4357/aac2da](https://doi.org/10.3847/1538-4357/aac2da)
- Sumiyoshi, K., Ishizuka, C., Ohnishi, A., Yamada, S., & Suzuki, H. 2009, *ApJ*, 690, L43, doi: [10.1088/0004-637X/690/1/L43](https://doi.org/10.1088/0004-637X/690/1/L43)
- Sumiyoshi, K., Yamada, S., & Suzuki, H. 2007, *ApJ*, 667, 382, doi: [10.1086/520876](https://doi.org/10.1086/520876)
- . 2008, *ApJ*, 688, 1176, doi: [10.1086/592183](https://doi.org/10.1086/592183)
- Sumiyoshi, K., Yamada, S., Suzuki, H., & Chiba, S. 2006, *PhRvL*, 97, 091101, doi: [10.1103/PhysRevLett.97.091101](https://doi.org/10.1103/PhysRevLett.97.091101)
- Sumiyoshi, K., Yamada, S., Suzuki, H., et al. 2005, *ApJ*, 629, 922, doi: [10.1086/431788](https://doi.org/10.1086/431788)
- Summa, A., Hanke, F., Janka, H.-T., et al. 2016, *ApJ*, 825, 6, doi: [10.3847/0004-637X/825/1/6](https://doi.org/10.3847/0004-637X/825/1/6)
- Summa, A., Janka, H.-T., Melson, T., & Marek, A. 2018, *ApJ*, 852, 28, doi: [10.3847/1538-4357/aa9ce8](https://doi.org/10.3847/1538-4357/aa9ce8)
- Suwa, Y., Sumiyoshi, K., Nakazato, K., et al. 2019, *ApJ*, 881, 139, doi: [10.3847/1538-4357/ab2e05](https://doi.org/10.3847/1538-4357/ab2e05)
- Swesty, F. D., Lattimer, J. M., & Myra, E. S. 1994, *ApJ*, 425, 195, doi: [10.1086/173974](https://doi.org/10.1086/173974)
- Szkudlarek, M., Gondek-Rosińska, D., Villain, L., & Ansorg, M. 2019, *ApJ*, 879, 44, doi: [10.3847/1538-4357/ab1752](https://doi.org/10.3847/1538-4357/ab1752)
- Togashi, H., Nakazato, K., Takehara, Y., et al. 2017, *NuPhA*, 961, 78, doi: [10.1016/j.nuclphysa.2017.02.010](https://doi.org/10.1016/j.nuclphysa.2017.02.010)
- Torres-Forné, A., Cerdá-Durán, P., Obergaulinger, M., Müller, B., & Font, J. A. 2019, *PhRvL*, 123, 051102, doi: [10.1103/PhysRevLett.123.051102](https://doi.org/10.1103/PhysRevLett.123.051102)
- Ugliano, M., Janka, H.-T., Marek, A., & Arcones, A. 2012, *ApJ*, 757, 69, doi: [10.1088/0004-637X/757/1/69](https://doi.org/10.1088/0004-637X/757/1/69)
- Vartanyan, D., Burrows, A., & Radice, D. 2019, *MNRAS*, 489, 2227, doi: [10.1093/mnras/stz2307](https://doi.org/10.1093/mnras/stz2307)
- Vitale, S., Lynch, R., Sturani, R., & Graff, P. 2017, *CQGra*, 34, 03LT01, doi: [10.1088/1361-6382/aa552e](https://doi.org/10.1088/1361-6382/aa552e)
- Walk, L., Tamborra, I., Janka, H.-T., & Summa, A. 2019, arXiv:1910.12971 [astro-ph, physics:hep-ph]. <https://arxiv.org/abs/1910.12971>
- Warren, M. L., Couch, S. M., O'Connor, E. P., & Morozova, V. 2019, arXiv:1912.03328 [astro-ph]. <https://arxiv.org/abs/1912.03328>
- Wiktorowicz, G., Belczynski, K., & Maccarone, T. J. 2013, arXiv:1312.5924 [astro-ph]. <https://arxiv.org/abs/1312.5924>
- Woosley, S., & Heger, A. 2007, *PhR*, 442, 269, doi: [10.1016/j.physrep.2007.02.009](https://doi.org/10.1016/j.physrep.2007.02.009)
- Woosley, S. E., Heger, A., & Weaver, T. A. 2002, *RvMP*, 74, 1015, doi: [10.1103/RevModPhys.74.1015](https://doi.org/10.1103/RevModPhys.74.1015)
- Woosley, S. E., & Weaver, T. A. 1995, *ApJS*, 101, 181, doi: [10.1086/192237](https://doi.org/10.1086/192237)
- Yasin, H., Schäfer, S., Arcones, A., & Schwenk, A. 2018, arXiv:1812.02002 [astro-ph, physics:nucl-ex, physics:nucl-th]. <https://arxiv.org/abs/1812.02002>